

BIOMECHANICS OF THE LENS CAPSULE

A Thesis

by

MARK RICHARD HEISTAND

Submitted to the Office of Graduate Studies of
Texas A&M University
in partial fulfillment of the requirements for the degree of
MASTER OF SCIENCE

August 2004

Major Subject: Biomedical Engineering

BIOMECHANICS OF THE LENS CAPSULE

A Thesis

by

MARK RICHARD HEISTAND

Submitted to Texas A&M University
in partial fulfillment of the requirements
for the degree of

MASTER OF SCIENCE

Approved as to style and content by:

Jay D. Humphrey
(Chair of Committee)

John C. Criscione
(Member)

Joan Dziezyc
(Member)

William A. Hyman
(Head of Department)

August 2004

Major Subject: Biomedical Engineering

ABSTRACT

Biomechanics of the Lens Capsule. (August 2004)

Mark Richard Heistand, B.S., Texas A&M University

Chair of Advisory Committee: Dr. Jay D. Humphrey

Knowledge of the mechanics of the lens capsule is crucial for improving cataract surgery as well as understanding better the physiological role of the lens capsule in the process of accommodation. Previous research on the mechanical properties of the lens capsule contains many gaps and contradictions due to experimental limitations and inappropriate assumptions. Thus, the goal of this work is to quantify fully the regional, multi-axial mechanical behavior of the lens capsule and to calculate the change in stress and strain fields as a result of cataract surgery.

Determining in situ the multi-axial mechanical behavior of the lens capsule required the design and construction of an experimental device capable of altering stresses in the capsule while measuring localized surface deformations. Tests performed on this device reveal that the meridional and circumferential strains align with the principal directions and are equivalent through most of the anterior lens capsule, except close to the equator where the meridional strain is greater. Furthermore, preconditioning effects were also found to be significant. Most importantly, however, these tests provide the data necessary for calculating material properties.

This experimental system is advantageous in that it allows reconstruction of 3D geometry of the lens capsule and thereby quantification of curvature changes, as well as

measurement of surface deformations that result from various surgical interventions.

For instance, a continuous circular capsulorhexis (CCC) is commonly used during cataract surgery to create a hole in the anterior lens capsule (typically with a diameter of 5 mm). After the introduction of a CCC, strain was found to redistribute evenly from the meridional direction (retractational strain) to the circumferential direction (extensional strain), where both directional components of strain reached magnitudes up to 20% near the edge of the CCC. Furthermore, the curvature was found to increase at the edge of the CCC and remain the same near the equator, indicating that the mere introduction of a hole in the lens capsule will alter the focal characteristics of the lens and must therefore be considered in the design of an accommodative intraocular lens.

ACKNOWLEDGMENTS

Funding for this project was provided by the State of Texas Medical Biotechnology ATP 000512-0097-2001 and Alcon Labs, Ft. Worth, TX. We enjoy working with Alcon and wish to thank them for their helpful guidance and cooperation. I would also like to personally thank my wife for her unending patience, support, and encouragement throughout my college career. Furthermore, I want to acknowledge Sherry Delange, Guido David, and Ryan Pedrigi for the help they have provided. I have enjoyed working closely with each of them. I would also like to thank Dr. Joan Dziezyc for her surgical expertise as well as her encouragement and interest in this project. Lastly, I want to express my deepest gratitude towards Dr. Jay Humphrey, in appreciation of his support and counsel during the course of my graduate studies. His passion for biomechanics is inspiring, and his strong work ethic is very motivating. Most importantly, I consider him a mentor and am very grateful for the opportunity to learn so much from him.

TABLE OF CONTENTS

		Page
ABSTRACT		iii
ACKNOWLEDGMENTS.....		v
TABLE OF CONTENTS		vi
LIST OF FIGURES.....		viii
CHAPTER		
I	INTRODUCTION	1
II	BACKGROUND.....	4
	Characteristics of the Lens Capsule.....	4
	Limitations of Current Mechanical Tests	6
	Present Needs.....	10
III	MULTIAXIAL MECHANICS OF THE LENS CAPSULE.....	12
	Specimen Preparation	12
	Experimental System	14
	Calibration	16
	Resolution	18
	Analysis.....	19
	3D Object Reconstruction.....	19
	Calculation of Strain.....	23
	Experimental Protocols.....	26
	Results.....	26
	Discussion.....	36
IV	STRAIN REDISTRIBUTION FROM CAPSULORHEXIS	39
	Experimental Methods	40
	Analysis.....	40
	Strain Calculation	40
	Curvature Calculation.....	42
	Results.....	49
	Discussion.....	58

CHAPTER	Page
V DISCUSSION	61
VI RECOMMENDATIONS	65
Calculation of Material Properties	65
Study of Posterior Capsule.....	67
Mathematical Modeling of Lens Capsule	67
Computing Regional Curvatures.....	69
Calculating Stress Resultants.....	69
Strain Redistribution from IOL.....	70
Accommodation.....	71
Studies on Human Lens Capsule	71
VII CONCLUSION.....	73
REFERENCES.....	76
VITA	80

LIST OF FIGURES

FIGURE	Page
1 Schematic of the lens and lens capsule illustrating the normal location of the epithelial cells and equatorial lens bow.....	6
2 H&E stained histological cross-section of the porcine lens with lens capsule (40x)	13
3 Cut-away schematic view of the top right quadrant of an anterior lens capsule showing typical marker arrangements, consisting of seven overlapping sets of five markers	14
4 Schema of the experimental system	15
5 Picture of calibration device with platform lowered into the bath	17
6 Reconstruction of 3D positions of markers on a calibration sphere	19
7 Illustration of the relationship between camera position and the mathematical concept of projection tensors	20
8 Plot of global 3D coordinates of markers on the anterior surface of a pressurized lens capsule	23
9 Standardized subdivision of each marker set into four groups of marker triplets for strain calculation	24
10 Schema of the lens capsule showing the directions for the different components of strain, which originate at the centroid of each marker triplet	24
11 Illustration of position vectors from a triplet of markers, necessary for calculating the deformation gradient.	25
12 Comparison of the projected strain approximation from our inflation test (New) with that of Delange (Old), for all four groups of marker set B from both tests.....	27

FIGURE	Page
13 Comparison of meridional, circumferential, and shear components of strain for the first and fifth cycle of pressurization to 40 mmHg, with respect to the in-situ unloaded reference configuration	28
14 Plot of all components of strain for marker set D during fifth cycle, with respect to the in-situ unloaded reference configuration	29
15 Plot of all components of strain for marker set F during fifth cycle, with respect to the in-situ unloaded reference configuration	30
16 Plot of loading and unloading curves from Set D of eight experiments	31
17 Plot of loading and unloading curves from Set D of eight experiments, where the strain is measured with respect to the pressure state at 10 mmHg	33
18 Plot of loading and unloading curves from Set G of eight experiments, where the strain is measured with respect to the pressure state at 10 mmHg.	34
19 Measured initial strains (strains at 10 mmHg with respect to the stress-free configuration) by region	35
20 Average loading and unloading data from set D of six experiments, shown with power curve of the form $y = Ax^b$, predicting strain values at pressure states that could not accurately be measured	36
21 Drawing that illustrates how the best “geometric fit” ellipsoid models the anterior lens capsule	48
22 Anterior Lens Capsule with field of markers in top-right quadrant immediately after surgical introduction of CCC with 5 mm diameter.....	50
23 Section of anterior lens capsule imaged with the experimental biplane video system; shown is a portion of marker field remaining after a CCC	50
24 Strain field in top-right quadrant of anterior lens capsule after introduction of CCC with 5 mm diameter. (Specimen: 1, Number of nodes: 39, Number of elements: 59)	52

FIGURE	Page
25 Strain field in top-right quadrant of anterior lens capsule after introduction of CCC with 5 mm diameter. (Specimen 2, Number of nodes: 38, Number of elements: 50)	53
26 Strain field in top-right quadrant of anterior lens capsule after introduction of CCC with 4.5 mm diameter. (Specimen 3, Number of nodes: 28, Number of elements: 42)	54
27 Strain field in top-right quadrant of anterior lens capsule after introduction of CCC with 3.5 mm diameter. (Specimen 4, Number of nodes: 53, Number of elements: 85)	55
28 Strain field in top-right quadrant of anterior lens capsule after introduction of CCC with 4 mm. diameter. (Specimen 5, Number of nodes: 21, Number of elements: 27)	56
29 Plot showing section of a quadric fit to marker coordinates before CCC	57
30 Estimates of the curvature along the major and minor axes of the anterior lens capsule, both before and after the CCC	58
31 Flowchart showing project organization	63

CHAPTER I

INTRODUCTION

A better understanding of the mechanics of the lens capsule and its physiological function is crucial for the treatment of many causes of visual impairment. One such loss in visual acuity is due to the formation of a cataract, which is a partial or complete opacity in the lens of the eye. Current statistics show that cataracts occur in more than one-half of Americans over 65 (American Academy of Ophthalmology, 2001). Removal of cataracts has now become the most frequently performed surgery in the U.S. (>1.5 million/yr), but in most cases the restoration of visual acuity is only temporary. Posterior capsule opacification (PCO) causes a secondary loss of visual acuity in up to 50% of all patients within 2-5 years after cataract surgery (Emery, 1999; Spalton, 1999).

Treatment of secondary cataracts costs Medicare over \$250 million per year and is the second most expensive surgical cost only behind that of the original cataract removal and implantation of an intraocular lens (IOL) (Apple et al., 2000). Secondary intervention by an Nd-YAG laser can itself result in further complications, such as raised intraocular pressure, damaged IOL, anterior chamber inflammation, and even retinal detachment (Spalton, 1999; Emery, 1999; Altamirano et al., 1992).

This PCO, or secondary cataract, primarily results from the epithelial cells migrating from the anterior lens capsule to the central region of the posterior lens capsule where they undergo epithelial-mesenchymal transition to fibroblastic-

This thesis follows the style and format of the Journal of Biomechanics.

myofibroblastic cell types (Marcantonio et al., 2000). This is characterized by an increased deposition of extracellular matrix (especially along the newly formed wrinkles in the posterior capsule resulting from the inserted IOL). Moreover, these cells primarily produce type IV collagen and laminin before cataract surgery but produce types I, III, V, and VI collagen, MMP-2 and MMP-9, TIMPs, and osteopontin after surgery (Saika et al., 2003). Furthermore, these post-transition cells are believed to proliferate and form large opaque bladder cells, occluding the visual axis (Apple et al., 2000). In addition to the increased proliferation, which may be stimulated by the cytokine TGF- β , there is an increased apoptosis.

Each aspect of the cell biology of PCO corresponds to either a typical wound healing response or a growth and remodeling response due to a mechano-stimulus. Ohata et al. (2001) show that lens epithelial cells are mechanosensitive, that is, they belong to the family of cells known as mechanocytes. Therefore, we hypothesize that secondary cataracts occur in part from the alteration in the mechanical environment of the epithelial cells on the lens capsule due to cataract surgery. Furthermore, reducing the occurrence of PCO will require a better understanding of the mechanotransduction pathways leading to altered epithelial cell function as well as quantification of changes in the native stress and strain fields of the lens capsule as a result of cataract surgery.

Another visual impairment, thought to be inflicted by age-related changes in the mechanics of the lens capsule, is presbyopia (Weale, 1963; Fisher, 1969b; Kaufman, 1992; Koretz, 1994). This occurs when the eye's accommodative function begins to diminish; then the eye can no longer focus between near and far objects. Understanding

the relative role of the lens capsule versus the elasticity of the lens substance in determining the shape of the lens in accommodation requires a detailed knowledge of the mechanical behavior of the native lens capsule. Recently, Weeber (1999) and Burd et al. (2002) have attempted numerical modeling of the accommodative function of the lens; however, their results suffered from the lack of qualified data on the geometric and material properties of the different components used in their accommodative model (namely the lens capsule, lens, and zonules). It is, therefore, necessary to quantify the mechanical properties of the lens capsule to better understand accommodation.

Ultimately, a greater knowledge of the biomechanics of the lens capsule will be useful in addressing a number of issues in ophthalmologic surgery and prosthetics, such as improved capsulotomy and extraction techniques for cataract removal, the proper design and insertion of IOLs, and the successful development of an accommodative lens.

CHAPTER II

BACKGROUND

Characteristics of the Lens Capsule

The lens capsule is a small, bag-like membrane that covers the lens of the eye. It is suspended in place by a system of suspensory ligaments, called ciliary zonules, and it maintains the lens in its proper shape and position. Shape changes of the lens can occur as a result of accommodation. During this process, it is understood that the ciliary muscles contract, thus relaxing tension in the suspensory ligaments and increasing curvature of the anterior surface of the lens, necessary for viewing short distances. Therefore, the lens capsule is in tension during negative accommodation (adjustment of the eye for long distances by relaxation of the ciliary muscle), and this tension plays a role in creating a pre-strain in the lens capsule. Research by Delange (2002) has quantified this pre-strain and has shown it to be higher in the radial direction (roughly 13%) as compared to the circumferential direction (roughly 8%).

The lens capsule is a basement membrane that consists primarily of type IV collagen (65% by dry weight) arranged in a fine 3D meshwork, with admixed adhesion molecules and proteoglycans (Barnard et al., 1992). Capsular tissue is deposited in a lamellar fashion at the inner surface and the mixing of newly formed collagen with collagen formed earlier does not occur (Young and Ocumpaugh, 1966; Rafferty and Goosens, 1978; Haddad and Bennett, 1988). It was also noted that, on occasion, the fine

branching matrix was more highly condensed in some areas (Barnard et al., 1992). From this we know that the lens capsule is heterogeneous with variable thickness.

In addition to heterogeneity, other material characteristics of the lens capsule have been theorized or experimentally determined. For instance, anisotropy appears evident from the ease at which the lens capsule tears in the circumferential direction, rather than the radial direction during cataract surgery. Furthermore, many have described the lens capsule as a highly nonlinear, elastic material. Recent studies, however, show that the lens capsule exhibits viscoelastic behavior on a short time-scale. Nevertheless, it is likely that this viscoelasticity is very small and can be neglected for most purposes.

Capsular thickness varies according to age and the location at which the measurements are taken (Salzmann, 1912; Fisher and Pettet, 1972; Seland, 1974; Travers, 1990). The anterior and posterior lens capsules are approximately 60 μm and 40 μm , respectively, in the porcine eye and 11-33 μm and 4-9 μm in the human eye (Krag et al., 1997a; Krag and Andreassen, 2003). One reason the anterior lens capsule is thicker than the posterior capsule is that it comprises a monolayer of cuboidally-shaped epithelial cells; these cells transition, near the equator, into the so-called equatorial bow cells (Fig. 1).

Presently, there is limited research examining the mechanical properties of the lens capsule; however, it does appear that the mechanical behavior is dependent on region, age, and gender (Fisher, 1969a; Krag et al., 1997a) as well as disease (Bailey et al., 1993). As noted by Krag and Andreassen (2003), the lens capsule continues to grow

throughout most of life, growing in thickness anteriorly (most markedly in the periphery) and increasing in surface area to adjust to the increasing volume of the lens. One of the most common diseases affecting the lens capsule is diabetes mellitus, in which the glycosylation reaction of type IV collagen in the lens capsule is accelerated several fold (Monnier et al., 1979; Cohen et al., 1980; Schnider and Kohn, 1980). This leads to a stiffening and thickening of the capsule (Andreassen et al., 1981), as well as an increased occurrence of PCO (Hayashi et al., 2002).

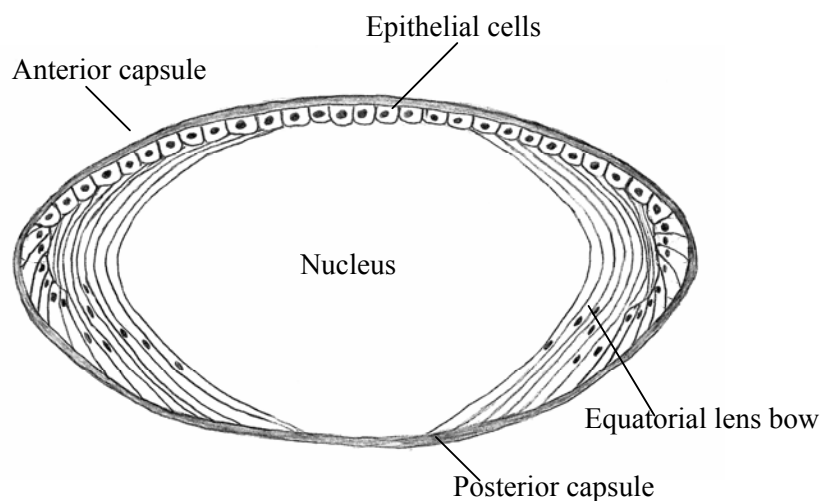


Fig. 1. Schematic of the lens and lens capsule illustrating the normal location of the epithelial cells and equatorial lens bow.

Limitations of Current Mechanical Tests

Effort has previously been made to quantify the mechanical properties of the lens capsule, yet there are many fundamental shortcomings that make most current data unusable. For instance, Fisher (1969a) used a volumetric strain method to quantitatively

investigate the mechanical behavior of the lens capsule; however, this procedure included several approximations concerning capsular porosity and the initial (unloaded) area of the test specimen, and maximal extension was found to be much less than surgical experience dictates. More recently, Krag et al. (1997a) used a uniaxial test procedure, but their 1-D extensibility test ruins the native geometry of the lens capsule and can not be extended to describe the multiaxial behavior of the lens capsule since it is most likely heterogeneous and anisotropic. Furthermore, both investigations were inappropriately based on linearized elasticity theory even though the lens capsule has been shown to behave nonlinearly. Moreover, they both neglected the effects of preconditioning, and they calculated stresses using average thickness measurements of the capsule, even though the thickness varies radially.

Research by Delange (2002) has overcome many of these limitations by collecting multiaxial data at several localized regions on the anterior lens capsule. Nevertheless, the effects of preconditioning were not considered, and information was not collected on the behavior of the lens capsule on the periphery, near the equator. Furthermore, regional geometry was not measured, so that localized curvature, and thus the in-plane stress resultants, could not be determined.

It also appears that discrepancies may be present in studies of the viscoelastic behavior of the lens capsule. Krag and Andreassen (2003) claim that the lens capsule exhibits viscoelastic properties, i.e. the mechanical response is time-dependent. They conclude this from the hysteresis between the loading and unloading of the lens capsule and the stress relaxation they found of approximately 12% at 10% strain and

approximately 21% at 40% strain after 20 seconds. On the other hand, Delange (2002) argues that the lens capsule behaves nearly elastically, as evident from reported creep tests in which no creep was observed after a dilatation pressure of 45 mmHg was quickly applied to the lens capsule (originally in its native state). Furthermore, the lens capsule has been classically regarded as an ideal elastic tissue, which is a reasonable assessment considering that any viscoelasticity of the lens capsule would likely require constant, accommodative adjustments of the eye to maintain focus on an object for a long period of time.

The results from these two studies may seem contradictory since creep and stress-relaxation are both attributed to viscoelasticity, yet only one phenomenon was observed. Nevertheless, it should be noted that stress-relaxation experiments measure the decrease in stress with time for a constant strain, while creep experiments measure the increase in strain with time for a constant load; thus, it is difficult to compare the two studies since they are both measuring different processes. Krag and Andreassen also used human lens capsules, while Delange used porcine lens capsules. Furthermore, discrepancies may arise due to certain limitations of each study. For instance, there are two problems in the testing technique used by Krag and Andreassen. First, they only loaded and unloaded the specimen once. This does not account for preconditioning effects, in which multiple loading cycles tend to stress soften (i.e. precondition) the material, as discussed by Mullins and Tobin (1957), so that subsequent cycles are consistent and more representative of the materials natural response. Most importantly, preconditioning has been shown necessary for many biological soft tissues (Fung, 1993),

and the small hysteresis (energy dissipation) exhibited by the lens capsule is expected to decrease after preconditioning. The second problem is that they did not test the lens capsule in its native state. They use an excimer laser to cut thin rings from the lens capsule, thus severing the 3D mesh work of collagen fibers in the lens capsule. The stress relaxation seen may be due in part to the reorienting of broken collagen fibers, which would not be seen if tested in its native state. Moreover, the heat generated from the laser may induce thermal damage of the lens capsule, so that its material properties may be altered from its native state. Additionally, limitations in the experimental system used by Delange (2002) include the inability to measure early creep response (within the first minute), even though Krag and Andreassen (2003) showed most stress relaxation to occur within 5 seconds. It should be noted, however, that creep is primarily a long term response, while stress-relaxation typically occurs over much shorter time scales. Therefore, it is difficult to state conclusively, from these two studies, whether or not the lens capsule exhibits significant viscoelastic behavior. It is possible that there is some short-term viscoelasticity, but more tests must be conducted to verify this.

Additionally, studies must be conducted to determine how the mechanics of the lens capsule change as a result cataract surgery. Previous experimental studies performed on human lens capsules show that the edge of the anterior capsulotomy is much stronger when a continuous circular capsulorhexis (CCC) is used instead of either the “can-opener technique” or diathermy (Assia et al., 1991; Krag et al., 1997b). Furthermore, data has also been obtained on haptic resistance forces from inserted IOLs,

but changes in stress and strain fields in the lens capsule, due to the introduction of a CCC or the insertion of an IOL, have not been examined.

Present Needs

As with any problem in mechanics, it is necessary to determine the geometry, material properties, and applied loads associated with the lens capsule. This information has not fully been captured through any single experiment by previous researchers. Furthermore, there appears to be many discrepancies in the small amount of data that has been collected. These shortcomings are primarily due to poorly designed experiments or inappropriate material models. Thus, there is a need to design a new experimental system appropriate for investigating in situ the regional, multiaxial mechanical behavior of the lens capsule, based on what is already known about its general characteristics (i.e., heterogeneity and anisotropy). Specifically, this new experimental system must provide a way to alter stresses in the lens capsule, while quantifying in-plane surface deformations in localized regions on the anterior pole as well as near the equator. Furthermore, it must allow for three-dimensional (3D) reconstruction of lens capsule geometry, thus overcoming previous inability to capture principal curvature measurements necessary for determining in-plane stress resultants.

There is also a need to quantify the material parameters of the lens capsule. Therefore, a constitutive framework, appropriate for nonlinear, pseudoelastic, biological membranes, must be used with experimental data collected from this new system to calculate material parameters. These parameters can then be used in computer simulations to predict strains, given specified loading conditions; this will ultimately aid

in the optimization of IOL design and improvement of surgical techniques used for cataract removal.

There is also a need to examine the redistribution of stress and strain fields in the lens capsule which occur as a result of cataract surgery. An experimental system allowing 3D reconstruction of lens capsule geometry is advantageous, in that it lends itself towards quantification of curvature changes and surface deformations resulting from various surgical procedures. Therefore, this system will give us a greater understanding of secondary cataracts and more insight into the possible mechanotransduction pathways causing their occurrence.

CHAPTER III

MULTIAXIAL MECHANICS OF THE LENS CAPSULE

As a result of the basic science and clinical observations reported in the literature, we hypothesize that cataract surgery perturbs the native stress and strain fields within the lens capsule; through mechanotransduction mechanisms, this perturbation stimulates the errant response by the epithelial cells. To test this hypothesis, we must first quantify the native stress and strain fields in the lens capsule and then compute or measure how these fields change due to various interventions and designs of intraocular implants. Toward this end, we must know the associated geometry, material properties, and applied loads. In this chapter, we present a new experimental approach for investigating, in situ, the multiaxial, mechanical behavior of the lens capsule in enucleated eyes. Further, we present the first detailed data on the regional, multiaxial, pseudoelastic behavior of the anterior porcine lens capsule.

Specimen Preparation

Fresh porcine eyes were received following an overnight shipment in iced saline from SiouxPreme, Inc. (Idaho). The cornea and iris were excised, and the globe was secured in a moldable wax fixture using multiple pins placed through the peri-scleral tissue. Next, we used a precision micro-manipulator to insert a 25-gauge needle just under the lens capsule. We applied a small amount of glue around the needle to seal the insertion site and then slowly injected a physiologic saline into the lens. In most cases, the fluid flowed out of and around the lens, thus separating large portions of the lens

capsule from the lens. Fig. 2 is an H&E stained cross-section of a lens capsule, shown in both a native and pressurized state; both were fixed via 24 hour immersion in 10% formaldehyde, with the pressurized lens capsule perfusion-fixed at 30 mmHg. As desired, the epithelial cells remained on the fluid-separated anterior capsule.

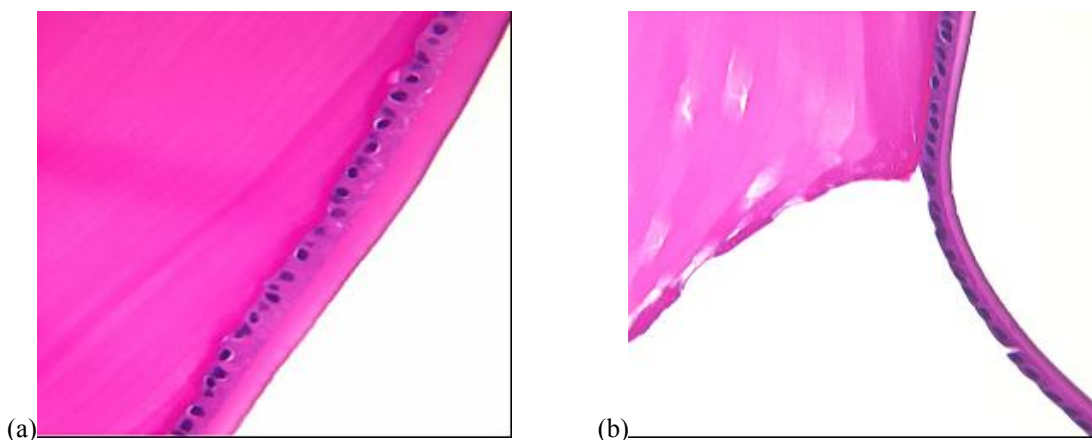


Fig. 2. H&E stained histological cross-section of the porcine lens with lens capsule (40x). (a) Anterior Lens capsule in its native state. (b) Pressure distended (30 mmHg) anterior lens capsule. Note the clean separation between the lens and lens capsule, as desired, and that the stretched epithelial cells remain on the anterior capsule.

Once the intact lens capsule was successfully separated from the underlying lens, multiple 40- μm diameter fluorescent, polystyrene microspheres (Bangs Laboratories, Fishers, IN), previously affixed to the surface of the anterior lens capsule, could then be imaged at different distention pressures. These microspheres serve as markers, locating the position of distinct points on the lens capsule; their hydrophobic nature and natural adhesion to type IV collagen prevents independent movement of the microsphere from the underlying lens capsule. These markers are arranged in sets of five (1 center marker and four corner markers), and these sets are then organized along the major and minor

axes of the lens capsule, spanning from the anterior pole to the periphery near the equator (Fig. 3). The anterior pole was anatomically determined as the point on the lens capsule directly above the intersection of the Y-suture lines in the lens. Note, too, that the markers were always placed on the side of the lens capsule opposite the inserted needle. Next, the eye was immersed in a physiologic solution (Alcon BSS) and warmed to 35°C. The specimen and specimen chamber were then moved into position for testing as described below.

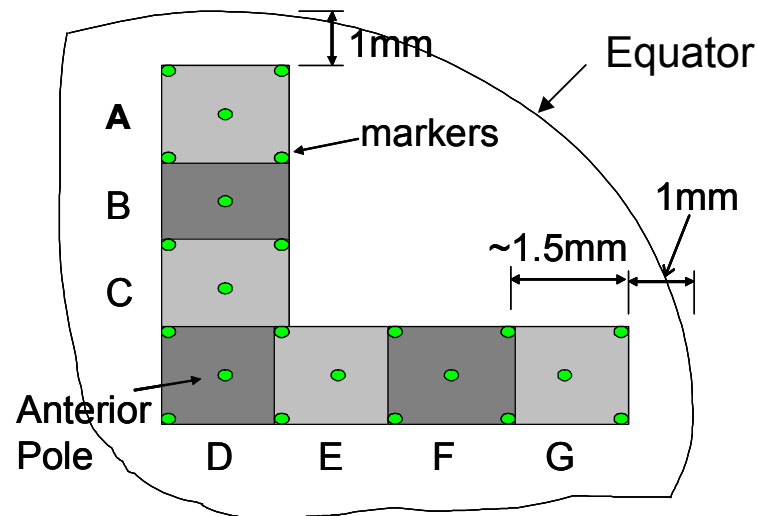


Fig. 3. Cut-away schematic view of the top right quadrant of an anterior lens capsule showing typical marker arrangements, consisting of seven overlapping sets of five markers.

Experimental System

Fig. 4 is a drawing of the optical-mechanical components of a custom biplane, video-based test system. It includes: an optical table, a linear railway and carriage with a micro-adjustable translation stage and attached needle-injection micro-manipulator, a Plexiglas specimen chamber, a pressure transducer, a fluorescent light source, and two

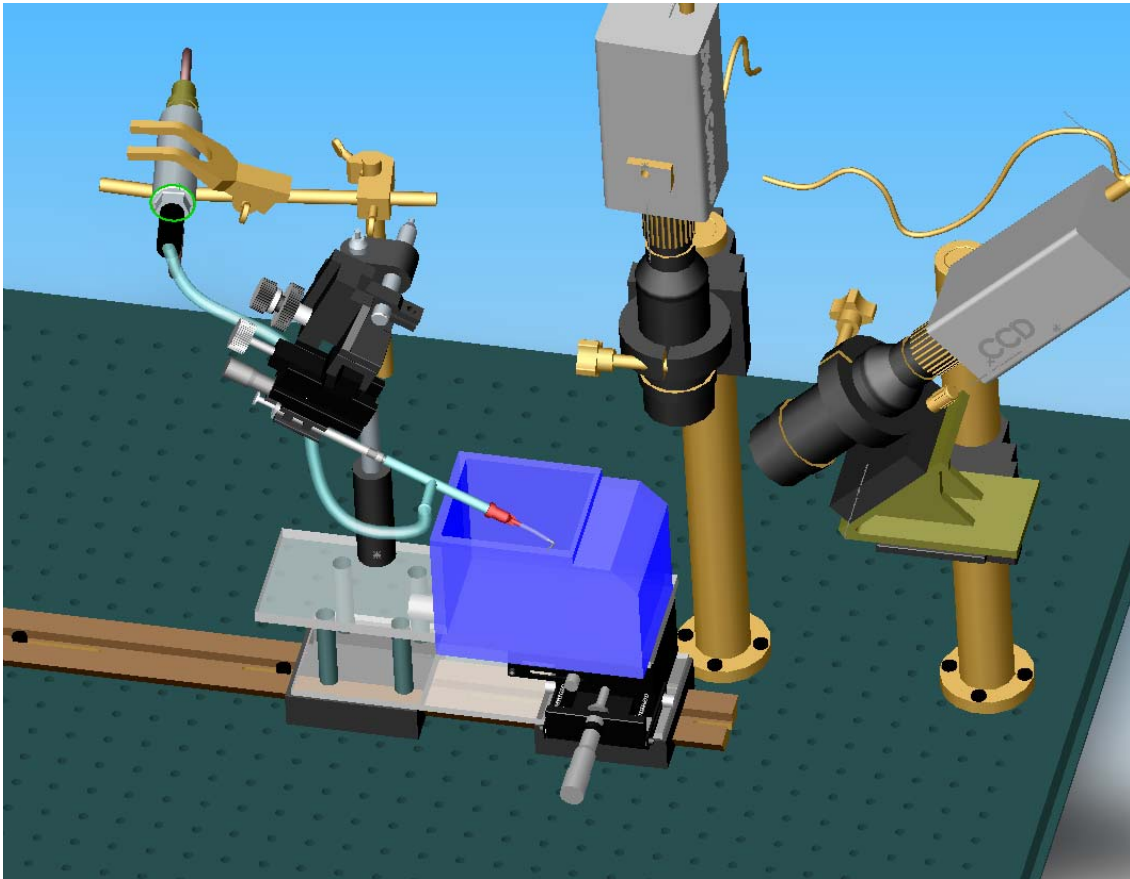


Fig. 4. Schema of the experimental system.

Sony CCD cameras, each outfitted with a long distance microscope lens (InfiniMax by Infinity Photo-Optical, Boulder, CO). Not shown are the operating microscope (to the left of the optical table), two B&W monitors, a temperature controller, a video-multiplexer and video cassette recorder, and a controller PC (with A/D and video frame-grabber boards). Note that the carriage-stage-needle-injection assembly can be translated as a rigid body along the railway, thus allowing the eye to be prepared under an operating microscope and then moved under the CCDs for mechanical testing while not disturbing the needle insertion within the eye.

The light source is a Jensen 150 Watt high-intensity, white light illuminator. It provides illumination of the specimen via dual channel fiber optic light guides, coupled with focusable lenses. A shortpass filter having a sharp cutoff wavelength of 500nm is mounted at the end of each light guide so the light source emits a deep blue color, ideal for exciting the fluorescent microspheres with excitation/emission maxima of 480/520nm. Broadband filters (CWL: 520nm, FWHM: 40nm) are mounted in front of each camera to filter out background light as well as reflected light from the light source.

The cameras are arranged so that one is directly above the specimen with its visual axis perpendicular to the optical table, while the other is placed in-plane, 45° apart from the first so their visual axes intersect at a 45° angle in a plane that is perpendicular to the optical table. The angled camera is mounted to a vertical translational stage so that the intersection of the visual axes can be moved up or down, allowing both cameras to image the same section of the specimen simultaneously. Furthermore, the cameras are each mounted to an additional translation stage to allow precise movement of each camera along its visual axis, thus providing independent focus adjustment.

Calibration

The two components of the experimental device requiring calibration are the pressure transducer and the biplane video system. The pressure transducer exhibits a linear relationship between output voltage and applied pressure; thus, it was easily calibrated using a mercury manometer and a fluid filled aspirator bottle. Pressure was supplied from the manometer between 0 and 70 mmHg in increments of 10 mmHg. Voltage for each pressure level was recorded from the pressure transducer using the

National Instruments A/D board and software. Voltage was plotted versus pressure, and the calibration constants were determined via linear regression. The video system requires the calculation of four calibration constants as discussed in the 3D Object Reconstruction section on page 19. These constants can be determined separately from the decoupled, linear calibration equations shown in Eq. 3. The details of the calibration procedure are given below.

First, a device was constructed which could be rigidly mounted to the optical table and could lower a platform into the bath (see Fig. 5). Note that the bath was designed with viewing surfaces orthogonal to the optical axis of each camera, thus

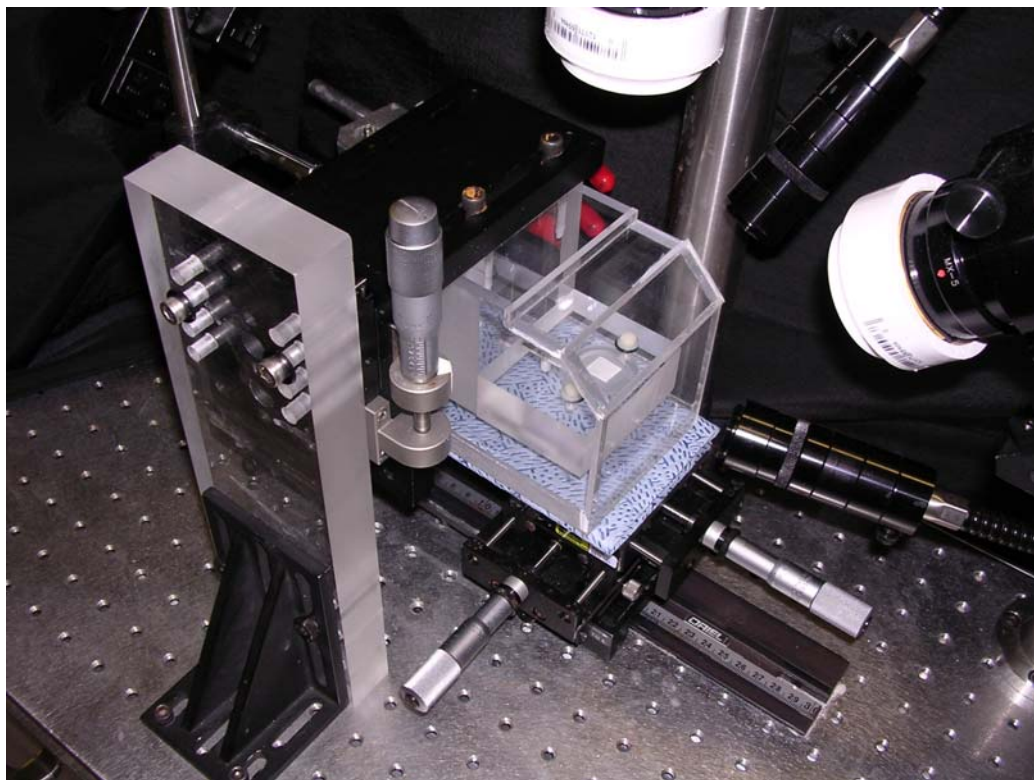


Fig. 5. Picture of calibration device with platform lowered into the bath.

avoiding refraction effects. The platform was parallel to the table and connected to a vertical translational stage, allowing precise control of its height. Attached to the top of the platform was a laser-etched 10mm by 10mm grid with lines spaced a quarter millimeter apart. The grid was brought into focus in both cameras, and the camera coordinates of six points (from intersecting grid lines) were determined for each camera. The grid was raised and then lowered 0.025 inches from its original height, still remaining within the depth of view for each camera, and six more points were measured at each new height. Calibration constants could then be determined using a linear least squares regression of the 18 data points for each of the calibration equations in Eq. 3.

Resolution

The resolution of the experimental system depends on that of the individual components. The pressure transducer is accurate to within $\pm 0.1\%$ full scale; current resolution is 0.05 mmHg. The image resolution for each camera is 130 pixels/mm, and the high-contrast images of fluorescent microspheres, coupled with the enhanced image filtering capabilities of the National Instruments IMAQ Vision software, allows us to measure the location of marker centroids to within less than a half pixel error. This was determined after placing approximately 50 markers on a 12 mm diameter tungsten carbide ball (illustrated in Fig. 6a) and calculating the camera coordinates of marker centroids five separate times. After using the calibration procedure, the three-dimensional position of each marker centroid could be determined in millimeters, with respect to a laboratory coordinate system (see Fig. 6b). The error in measuring the distance between two points, approximately 2 mm apart, was found to be less than 0.4%.

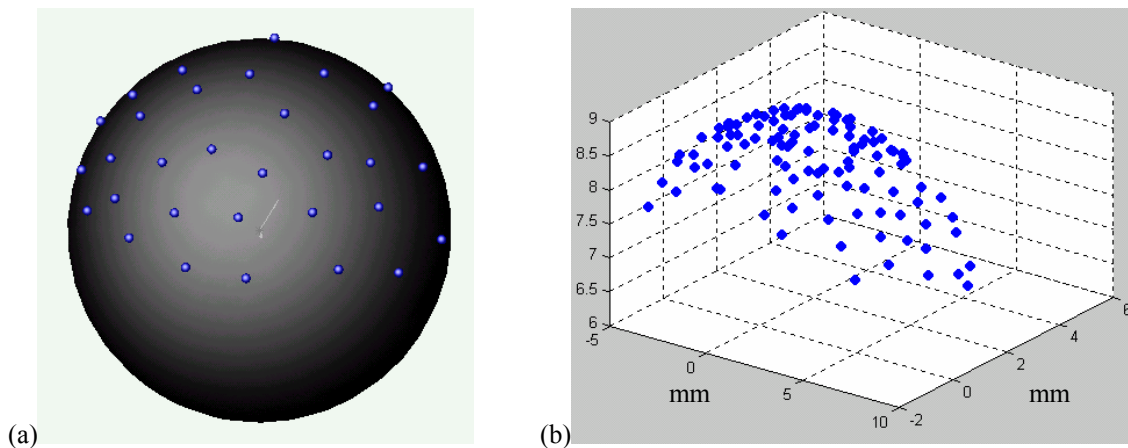


Fig. 6. Reconstruction of 3D positions of markers on a calibration sphere. (a) Drawing of markers on a 12 mm diameter tungsten carbide ball. (b) Reconstruction of marker position using biplane video system.

This was determined by rotating a calibration grid 15 times such that two points of known distance were always in view of both cameras. The 3D coordinates of the two points were found through spatial reconstruction from camera images, and the distance calculated between the points was typically within 0.2% error but never more than 0.4% error. Further error results since we are measuring changes in distances between points on a curved surface. This error is discussed by Delange (2002); a simple simulation was performed in which it was found that markers placed 2 millimeters apart on a uniformly inflating sphere produce an error of 0.47% because the changing length between the markers is merely an approximation of the changing arc length. Considering all sources of error, our biplane video system still provides a measure of strain within 1% error.

Analysis

3D Object Reconstruction

Global reconstruction techniques can be used with the biplane video system to rebuild three-dimensional objects from two separate, two-dimensional images of the

object. The process is simplified in our case since we are imaging microspheres and mapping the camera coordinates of their centroids into point space. Therefore, our system must provide a way for us to determine the location of an arbitrary point in a three-dimensional (3D) Euclidean space, given two separate camera views of a marker with its centroid located at that point. This can be described mathematically as finding the 3D coordinates of a point \mathbf{p} with respect to two orthogonal coordinate systems given by unit vectors $[\mathbf{e}, \mathbf{f}, \mathbf{g}]$ and $[\mathbf{e}^*, \mathbf{f}^*, \mathbf{g}^*]$, where the projection tensors $\mathbf{P}_1 = \mathbf{I} - \mathbf{g} \otimes \mathbf{g}$ and $\mathbf{P}_2 = \mathbf{I} - \mathbf{g}^* \otimes \mathbf{g}^*$ operate on \mathbf{p} to give the perpendicular projections onto the viewing planes of the two cameras as shown in Fig. 7.

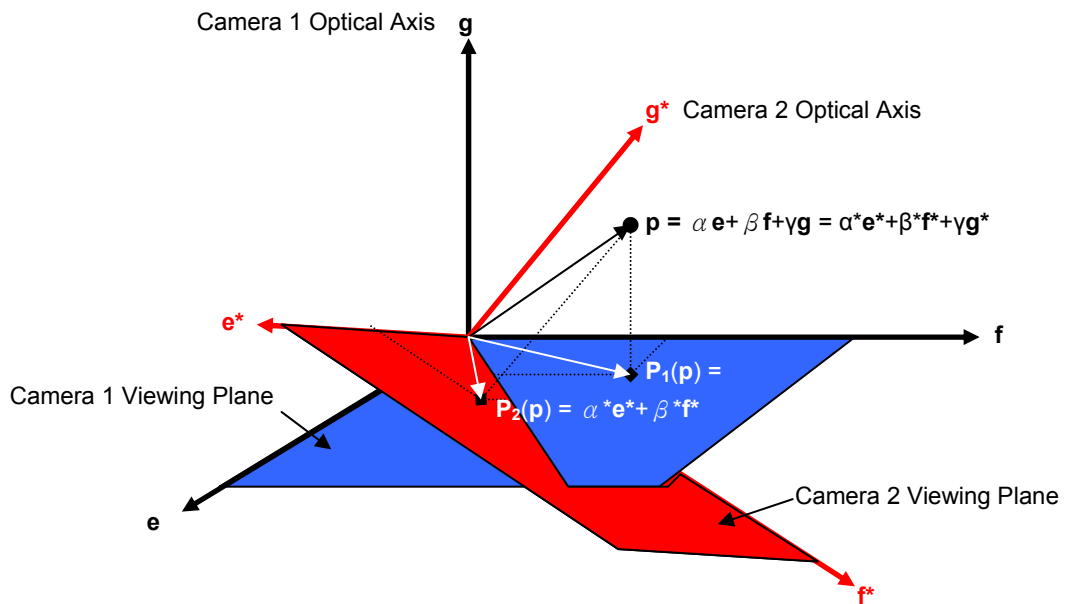


Fig. 7. Illustration of the relationship between camera position and the mathematical concept of projection tensors. Coordinates of a point viewed by each camera is represented by the perpendicular projection of the point onto a plane orthogonal to the optical axis of the camera.

We assume a linear relationship between image coordinates and the spatial location of a point \mathbf{p} (centroid of a marker), thus determination of 3D coordinates for a given point requires calculation of the twelve constants in the transformation equation

$$N_i^{(j)} = A_{ik}^{(j)} X_k^{(j)}, \quad (k \text{ sum } 1 \text{ to } 3). \quad (1)$$

From the above equation, N_i is the coordinate of a point from each camera in pixels, with $j = 1, 2$ indicating the camera and $i = 1, 2$ indicating the 2D y and x directions, respectively. The twelve calibration constants are given by $A_{ik}^{(j)}$, and the 3D Cartesian coordinates are given by $X_1^{(j)}, X_2^{(j)}, X_3^{(j)}$ with respect to the orthogonal basis vectors $[\mathbf{e}, \mathbf{f}, \mathbf{g}]$ for $j = 1$ and $[\mathbf{e}^*, \mathbf{f}^*, \mathbf{g}^*]$ for $j = 2$ (see Fig. 7).

The cameras are aligned with the orthogonal basis vectors such that N_1 does not depend on X_2 and N_2 does not depend on X_1 . Furthermore, the lenses provide constant magnification through the depth of view, thus N_i do not depend on X_3 ; this reduces the number of calibration constants to four. Our video system is also orientated so that one camera view is known relative to the second (in Fig. 7, $\mathbf{e} = \mathbf{e}^*$ and \mathbf{g}^* is rotated $\theta = 45^\circ$ clockwise from \mathbf{g}), thus $X^{(1)}$ and $X^{(2)}$ are related by the coordinate transition matrix

$$\begin{bmatrix} X_1^{(2)} \\ X_2^{(2)} \\ X_3^{(2)} \end{bmatrix}_{\mathbf{e}^*, \mathbf{f}^*, \mathbf{g}^*} = \begin{bmatrix} 1 & 0 & 0 \\ 0 & \cos \theta & -\sin \theta \\ 0 & \sin \theta & \cos \theta \end{bmatrix} \begin{bmatrix} X_1^{(1)} \\ X_2^{(1)} \\ X_3^{(1)} \end{bmatrix}_{\mathbf{e}, \mathbf{f}, \mathbf{g}}. \quad (2)$$

The four calibration constants (rewritten as B_i for $i = 1$ to 4) can be found with respect to a single set of basis vectors by individually solving the decoupled equations

$$\begin{aligned} N_1^{(1)} &= B_1 X_1 & N_1^{(2)} &= B_3 X_1 \\ N_2^{(1)} &= B_2 X_2 & N_2^{(2)} &= B_4 (X_2 \cos \theta - X_3 \sin \theta) \end{aligned} \quad (3)$$

for known camera coordinates N_i of imaged points with known spatial coordinates X_k , where the 3D Cartesian coordinates given by X_k are taken with respect to the orthogonal basis vectors $[\mathbf{e}, \mathbf{f}, \mathbf{g}]$. Once these constants are found, they can be used in the same equations to solve for the 3D coordinates of markers on the surface of the lens capsule, given camera coordinates (from both cameras) of each marker's centroid.

The camera coordinates of a marker centroid were calculated from digitized images using a custom code developed with National Instruments IMAQ Vision software. Coordinates for each centroid were returned in pixel values, indicating their respective location in the pixel domain of the 640 by 480 digitized image.

In addition, we are interested in finding the 3D coordinates of all marker centroids relative to each other. That is, we must calculate the 3D global coordinates of each centroid with respect to some arbitrary laboratory origin. This requires the camera coordinates of each centroid to be taken with respect to a common point, but the field of view for each camera is not wide enough to simultaneously capture all the markers. Therefore, several overlapping images were taken such that subsequent images involved a calculated translation of the stage and contained at least one marker shown in the previous image. The images were then stitched together to form a montage so that coordinates for each marker were with respect to a common point. The 3D reconstruction method discussed above could then be used to calculate the global 3D Cartesian coordinates of all markers; this yielded coordinates in millimeters, with respect to an origin chosen at the anterior pole (see Fig. 8).

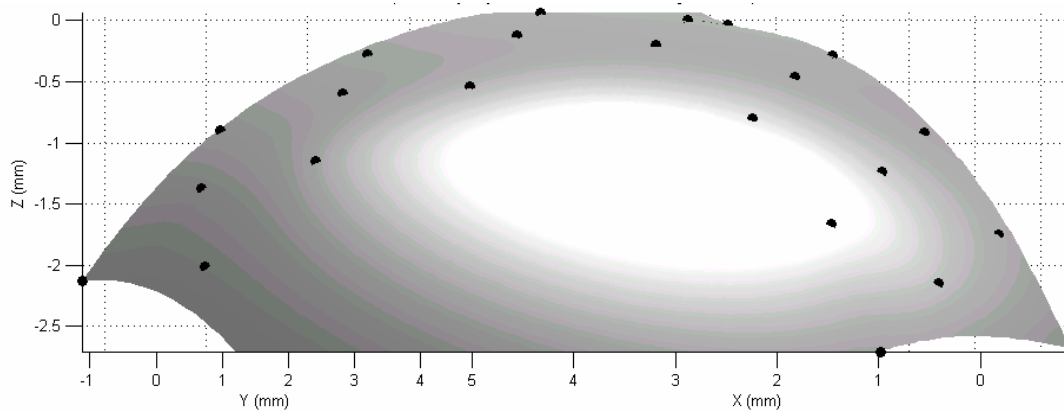


Fig. 8. Plot of global 3D coordinates of markers on the anterior surface of a pressurized lens capsule (surface shown is fitted to marker coordinates using biharmonic spline interpolation functions; the surface, with computer-generated lighting effects, is displayed for visualization purposes only).

Calculation of Strain

Monitoring the 3D kinematics of markers on the surface of the inflating lens capsule permits one to calculate the associated displacement gradients, and in turn, regional Green strains of the capsule. The specific arrangement of markers in sets of five allows for the construction of four triangles of similar size and shape in each set (see Fig. 9), where the corners of each triangle constitute a triplet of markers. A triplet of markers is the minimum set needed for calculating all three in-plane components of strain (Humphrey, 2002).

Finite Green strains, \mathbf{E} , were computed locally for each triplet using the deformation gradient, \mathbf{F} , through the equation $\mathbf{E} = \frac{1}{2}(\mathbf{F}^T\mathbf{F} - \mathbf{I})$. The three components of in-plane strain for each marker triplet are labeled as meridional, circumferential, and shear; the origin of the localized strain region was prescribed to be at the centroid of the triplet. The meridional component of strain always points to the anterior pole of the lens capsule and is tangent to the capsule at the triplet centroid. In addition, the

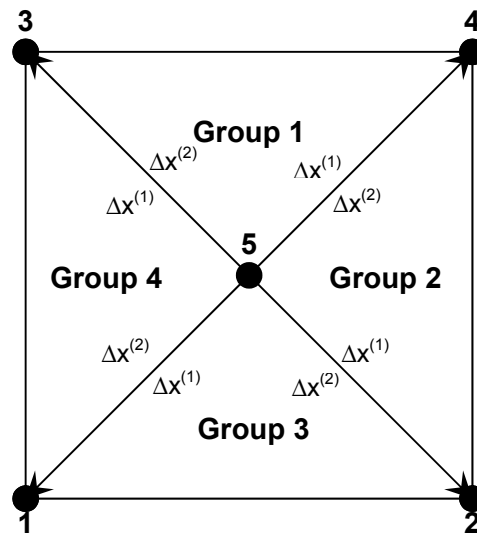


Fig. 9. Standardized subdivision of each marker set into four groups of marker triplets for strain calculation.

circumferential direction is tangent to the lens capsule at the centroid of the triplet and is perpendicular to the meridional direction, as illustrated in Fig. 10.

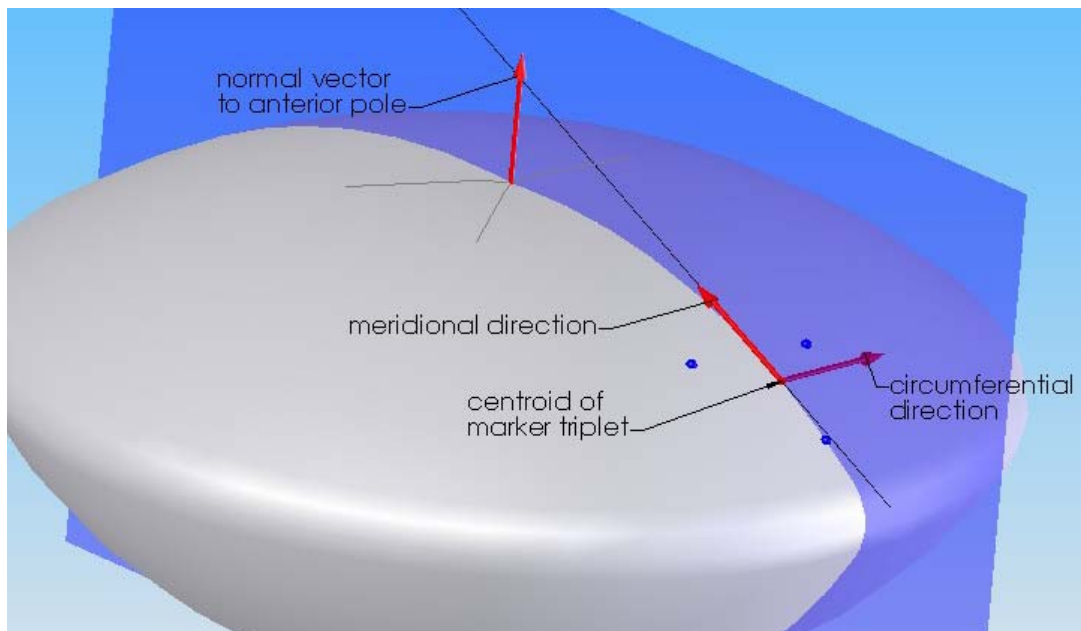


Fig. 10. Schema of the lens capsule showing the directions for the different components of strain, which originate at the centroid of each marker triplet.

The deformation gradient can be calculated directly for each marker triplet by finding how position vectors ($\Delta\mathbf{X}^{(1)} = \mathbf{X}^B - \mathbf{X}^A$ and $\Delta\mathbf{X}^{(2)} = \mathbf{X}^C - \mathbf{X}^A$) in the reference configuration, β_o , deform to position vectors ($\Delta\mathbf{x}^{(1)} = \mathbf{x}^b - \mathbf{x}^a$ and $\Delta\mathbf{x}^{(2)} = \mathbf{x}^c - \mathbf{x}^a$) in subsequent configurations, β_t , representing various inflated pressure states (e.g., Fig. 11). Since the marker triplets are close together and there are no severe deformation gradients, we can assume a homogeneous deformation within each triangular region created by a marker triplet. Thus, $\Delta\mathbf{x} \approx \mathbf{F}(\Delta\mathbf{X})$ and the in-plane components of \mathbf{F} can be solved for each pressure state using the matrix equation

$$\begin{bmatrix} \Delta x_1^{(1)} & \Delta x_1^{(2)} \\ \Delta x_2^{(1)} & \Delta x_2^{(2)} \end{bmatrix} = \begin{bmatrix} F_{11} & F_{12} \\ F_{21} & F_{22} \end{bmatrix} \begin{bmatrix} \Delta X_1^{(1)} & \Delta X_1^{(2)} \\ \Delta X_2^{(1)} & \Delta X_2^{(2)} \end{bmatrix}. \quad (4)$$

Note the standardized calculation of position vectors illustrated in Fig. 9 for each marker set, where all position vectors originate at the center marker of the set.

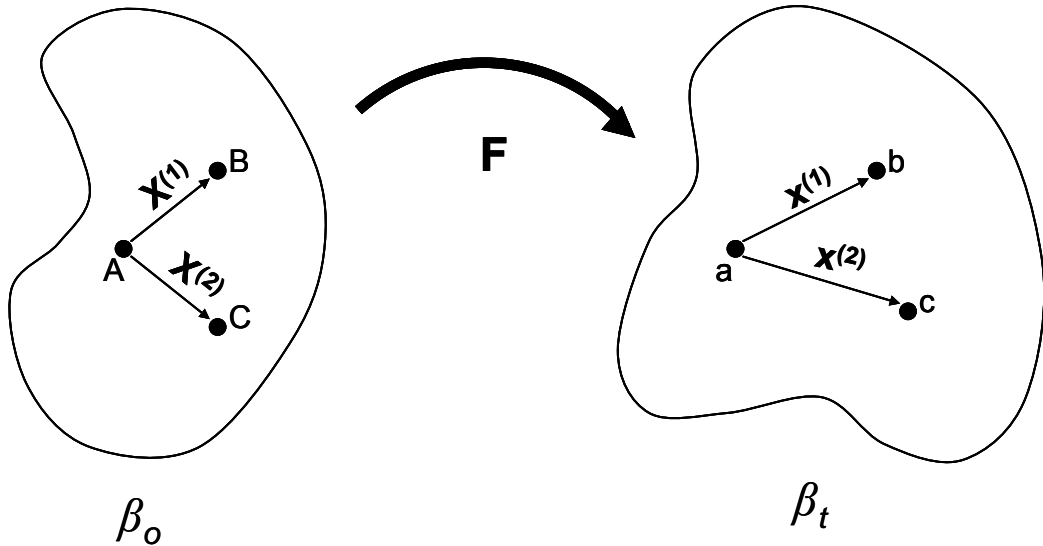


Fig. 11. Illustration of position vectors from a triplet of markers, necessary for calculating the deformation gradient.

Experimental Protocols

The specimen was pressurized slowly by raising a reservoir via a pulley system. The reservoir contained BSS solution and was connected to the pressure transducer and inserted needle, thus allowing control of the inflation pressure. The lens capsule was inflated in increments of 5 mmHg, with two minutes at each pressure state, so as to cycle the pressure from 0 to 45 to 0 mmHg five times. Images of all markers were collected at each pressure state during the first and fifth loading and unloading cycles. The final aspect of the experimental procedure involved obtaining a nearly stress-free configuration. This was accomplished by isolating the lens capsule and lens from the eye and then cutting the posterior lens capsule away to allow free movement of the anterior capsule. The markers were then imaged as the anterior lens capsule rested freely on the lens.

Results

Images of the inflating lens capsule from the camera perpendicular to the table (see Fig. 4), can be used to calculate projected strain approximations at different pressure states. These data should theoretically reproduce those of the inflation tests performed by Delange (2002). As shown in Fig. 12 our projected strain data from the first cycle of an inflation test does match well with previously reported inflation tests.

More importantly, images from both cameras of the biplane video system can be used to develop more accurate surface strain measurements. Fig. 13 shows the typical surface strain response of the lens capsule for loading and unloading during the first and fifth cycle, with respect to the in-situ, unloaded reference configuration (native state).

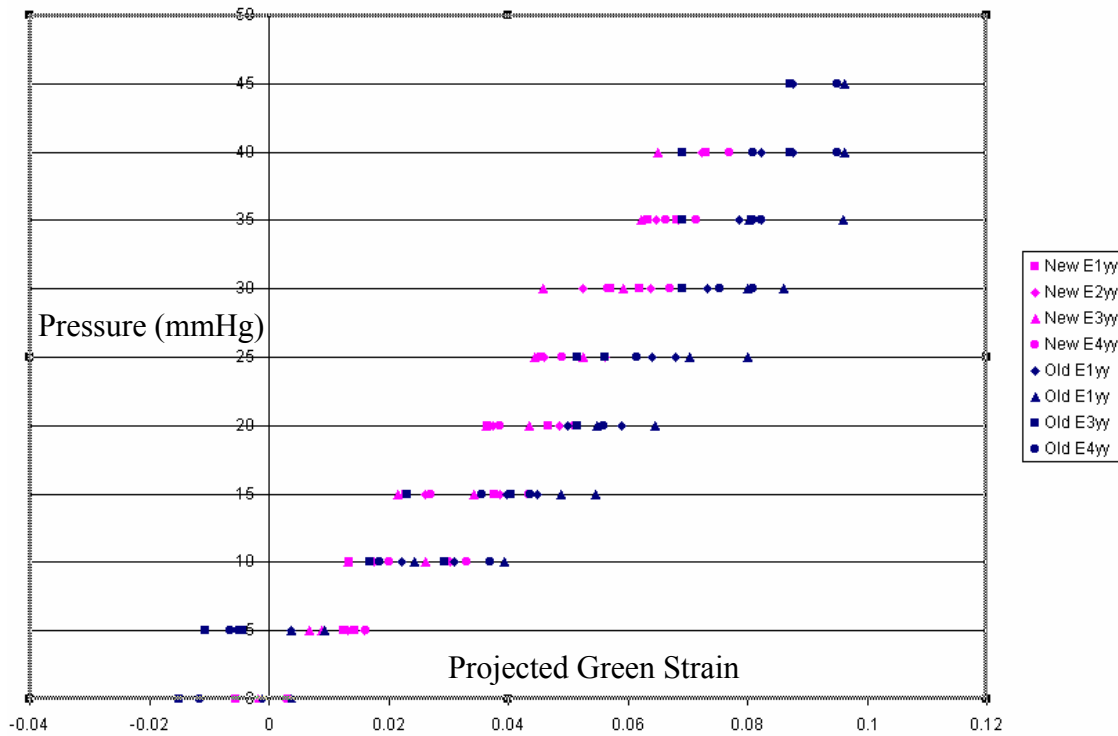


Fig. 12. Comparison of the projected strain approximation from our inflation test (New) with that of Delange (Old), for all four groups of marker set B from both tests (recall Fig. 3 for set specification). The strain is measured in the y-direction (roughly meridional direction for set B) of a laboratory coordinate system, which is chosen to be the same in both experiments.

Note the slight increase in strain magnitude and decrease in hysteresis of the fifth cycle compared to the first cycle; both indicate a notable preconditioning effect. Furthermore, the surface strains are greater than those found previously from the projected strain approximation for two reasons. First, a single camera is not capable of capturing motions along its optical axis. In this case, the camera perpendicular to the table was not able to measure the vertical displacements that are known to exist as a result of inflation, thus underestimating strain. Second, preconditioning effects were neglected for the projected strain approximation, even though preconditioning is known to “stress soften” biological tissue as evident for the anterior lens capsule in Fig. 13.

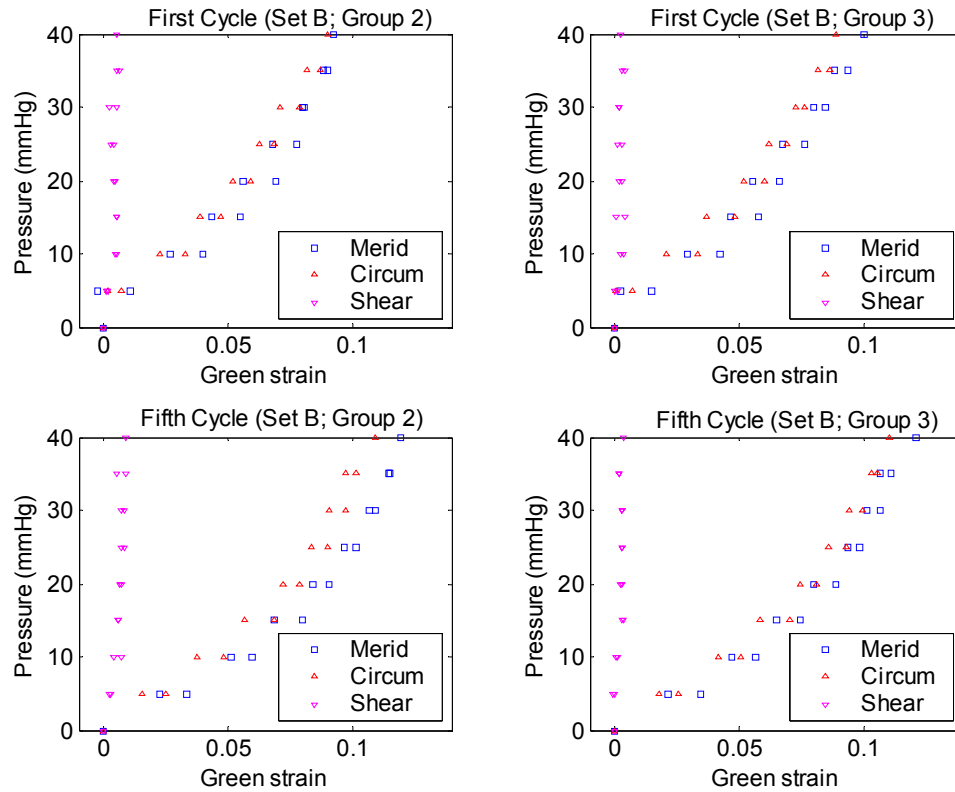


Fig. 13. Comparison of meridional, circumferential, and shear components of strain for the first and fifth cycle of pressurization to 40 mmHg, with respect to the in-situ unloaded reference configuration (see Fig. 3 and Fig. 9 for the location of each marker triplet).

Figs. 14 and 15 show pressure-strain data at the anterior pole (Set D) and near the equator (Set F) for all groups during the fifth cycle. The responses are nonlinear in the meridional and circumferential directions and approximately zero for shear in all four groups of both marker sets. This is an important observation for it reveals that the meridional and circumferential directions are principal directions. The meridional component of strain also appears to be greater than the circumferential component near the equator, but almost the same at the anterior pole. The directional components of strain at 40 mmHg, with respect to the native state, are typically around 10-12%.

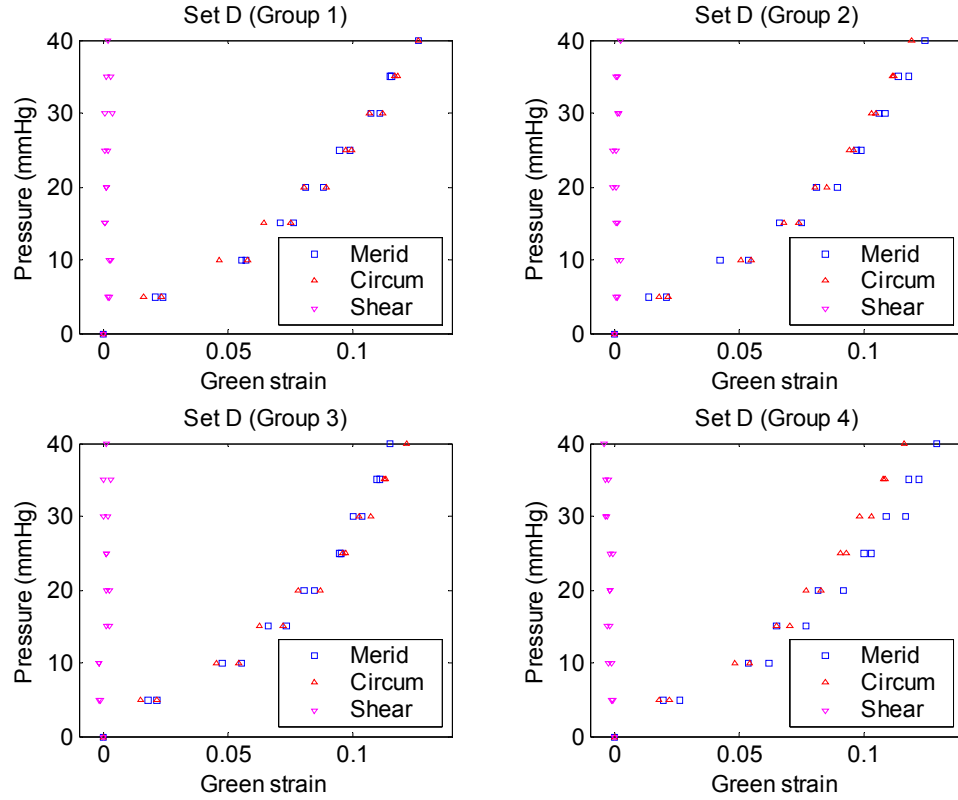


Fig. 14. Plot of all components of strain for marker set D during fifth cycle, with respect to the in-situ unloaded reference configuration. Note the consistency amongst the four sets of data within the region, thus supporting the computational assumption of local homogeneity. Furthermore, the near equibiaxial strains suggest a symmetry about the apex of the capsule.

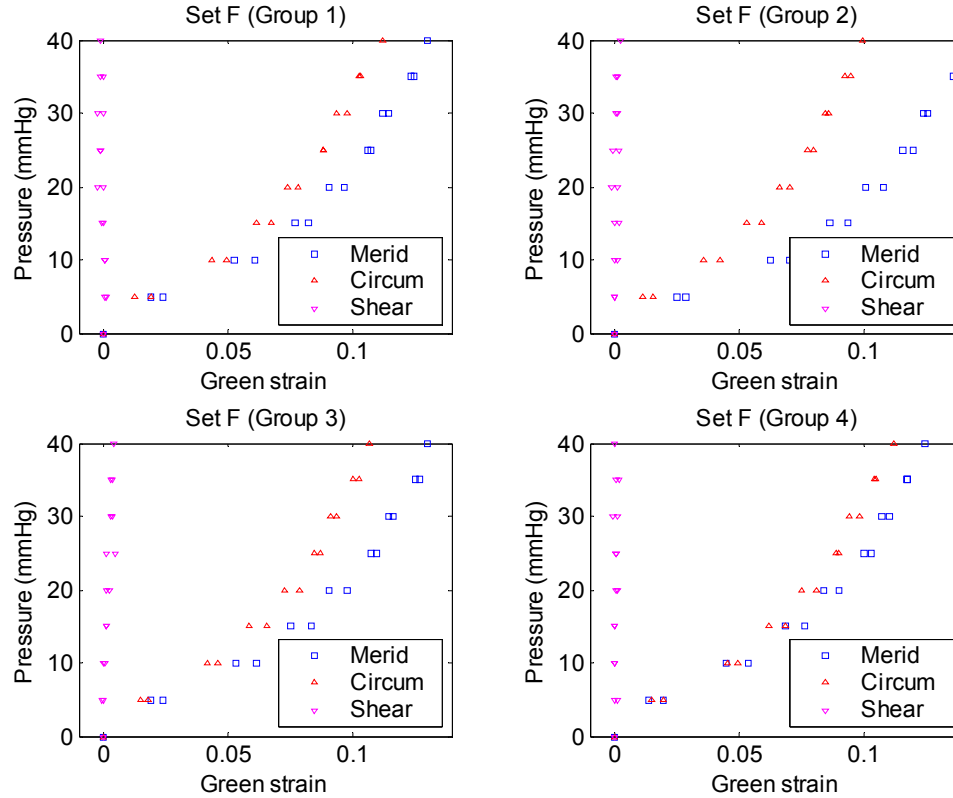


Fig. 15. Plot of all components of strain for marker set F during fifth cycle, with respect to the in-situ unloaded reference configuration. Note that the strains are greater in the meridional than the circumferential direction. This is consistent with a circumferential constraint at the equator. Indeed, note that the directional difference is greatest in group 2, as expected, which is closest to the equator.

Strains with respect to the zero pressure state in the meridional and circumferential directions from Set D, for eight specimens, are shown in Fig. 16. The shapes of the loading and unloading curves are similar for each specimen, but some appear to be horizontally shifted. We noted, however, that the lens capsule did not appear to inflate correctly from 0 to 10 mmHg for some of the experiments. It is possible that unknown interactions between the needle, lens, and lens capsule caused difficulties in obtaining low pressure states. Nevertheless, from an experimental point of

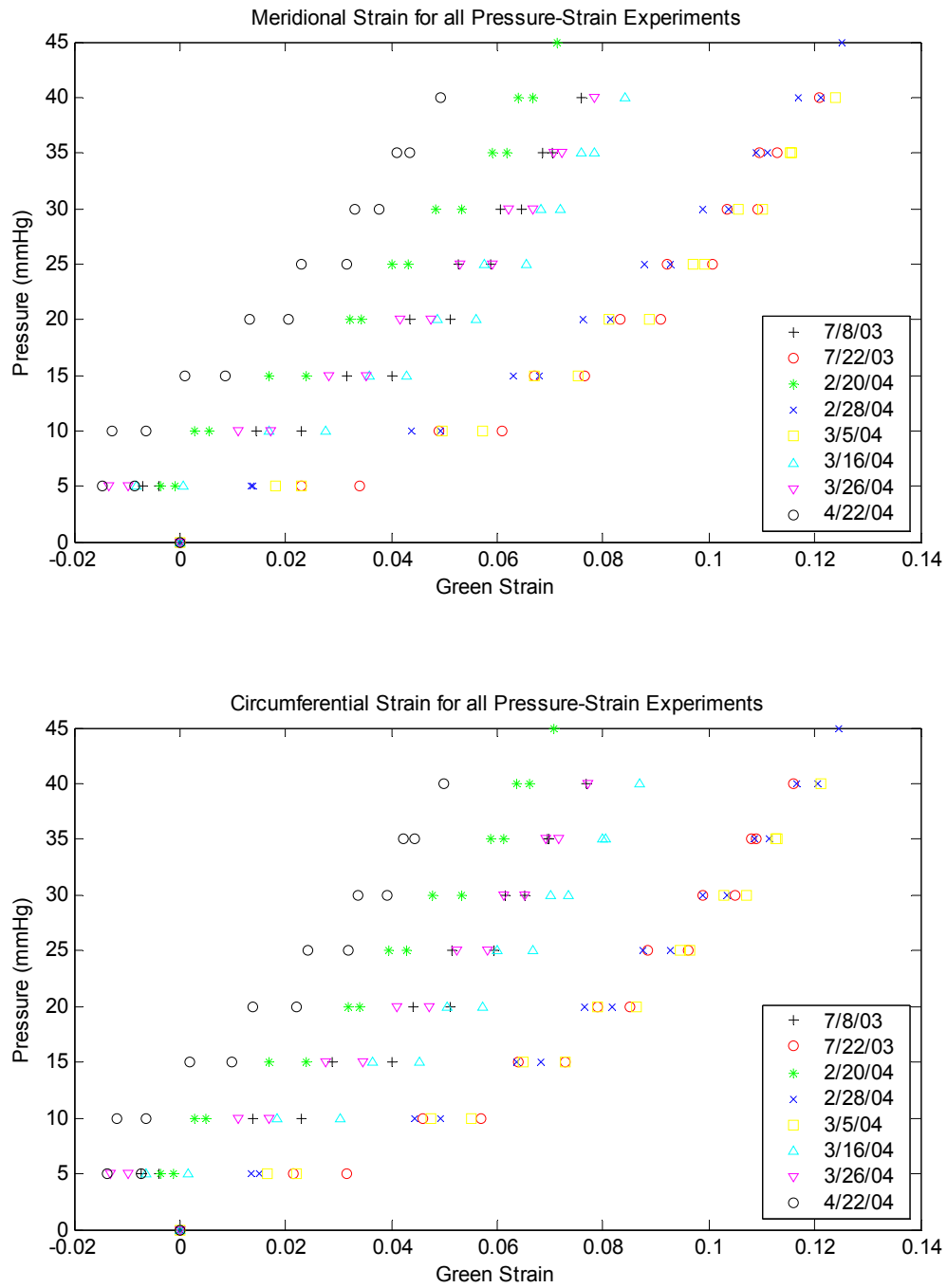


Fig. 16. Plot of loading and unloading curves from Set D of eight experiments.

view, a pressure state of 10 mmHg or higher is more appropriate as a reference for measuring strain.

Strains were then re-plotted with respect to the 10 mmHg pressure state in the meridional and circumferential directions from Set D and Set G, for eight specimens, as shown in Fig. 17 and Fig. 18, respectively, where the solid line indicates the average loading and unloading for all specimens pressurized to 40 mmHg. Of most importance, the loading and unloading curves for each specimen are now almost identical, thus verifying repeatability of our experimental method for inflation pressures above 10 mmHg. Note in Fig. 17 and Fig. 18 that the initial strain at 10 mmHg is assumed to be roughly 12%. This is found from the average measure of strain at 10 mmHg with respect to the stress-free reference configuration. Fig. 19 shows this initial strain for the different regions from three separate experiments. Therefore, the strain at 40 mmHg with respect to the stress-free, reference configuration was roughly 18-19% (see Fig. 17 and Fig. 18), owing to a pre-strain (strain in its in-situ, unloaded state compared to its stress-free state) of roughly 8% in the circumferential direction and 13% in the meridional direction (Delange, 2002).

If the average loading and unloading pressure-strain data from all specimens is plotted with respect to the stress-free reference configuration, the true shape of the strain curve is more apparent as shown in Fig. 20. Although this is not a stress-strain plot, a power curve can be fit to the loading and unloading data separately, revealing the highly nonlinear behavior of the lens capsule.

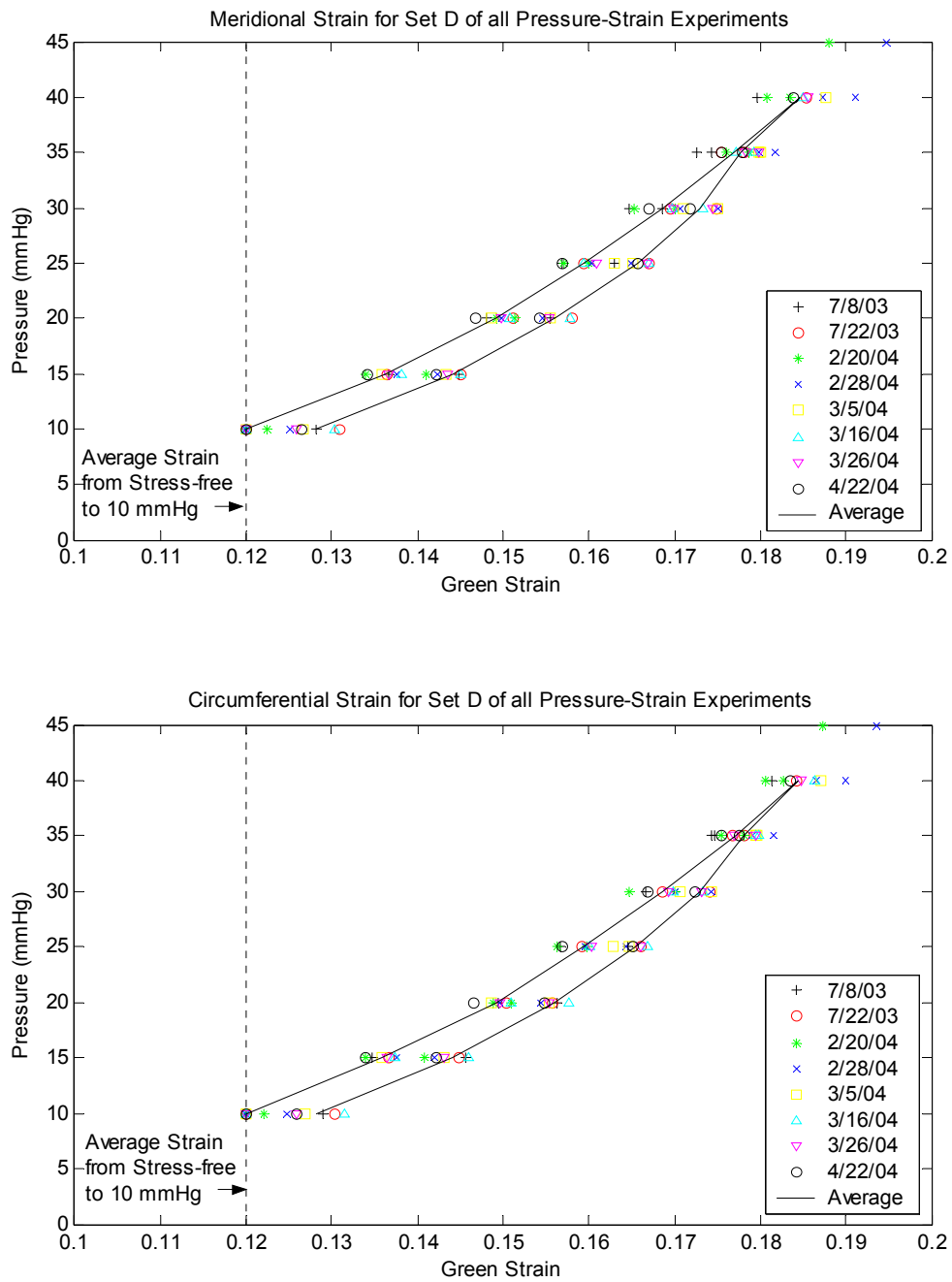


Fig. 17. Plot of loading and unloading curves from Set D of eight experiments, where the strain is measured with respect to the pressure state at 10 mmHg. The initial strain (at 10 mmHg) is assumed to be roughly 12%, which is the average strain calculated from the stress-free configuration to the 10 mmHg pressure state. Note the consistency of the data, demonstrating the repeatability of our experimental method.

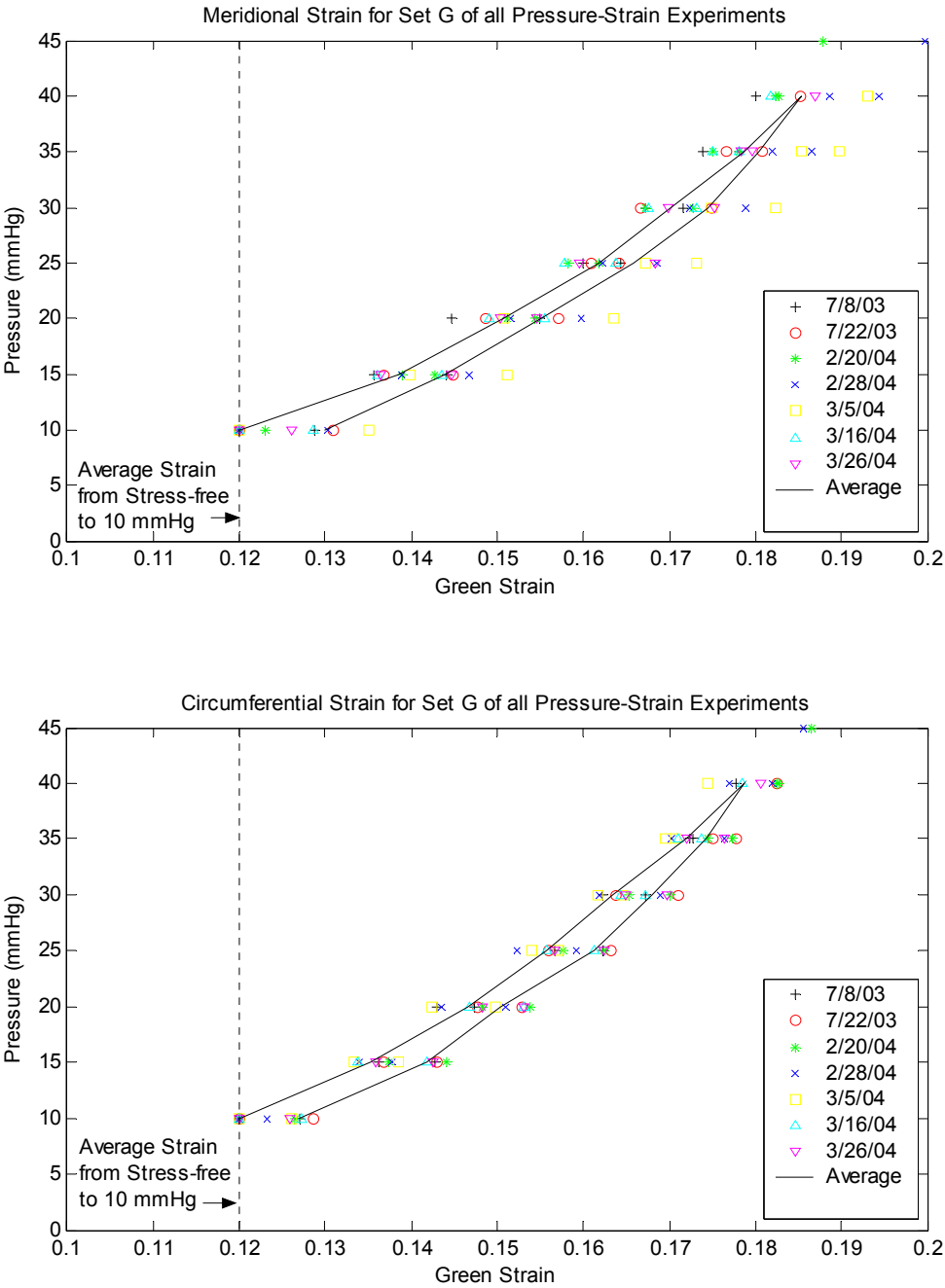


Fig. 18. Plot of loading and unloading curves from Set G of eight experiments, where the strain is measured with respect to the pressure state at 10 mmHg. The initial strain (at 10 mmHg) is assumed to be roughly 12%, which is the average strain calculated from the stress-free configuration to the 10 mmHg pressure state.

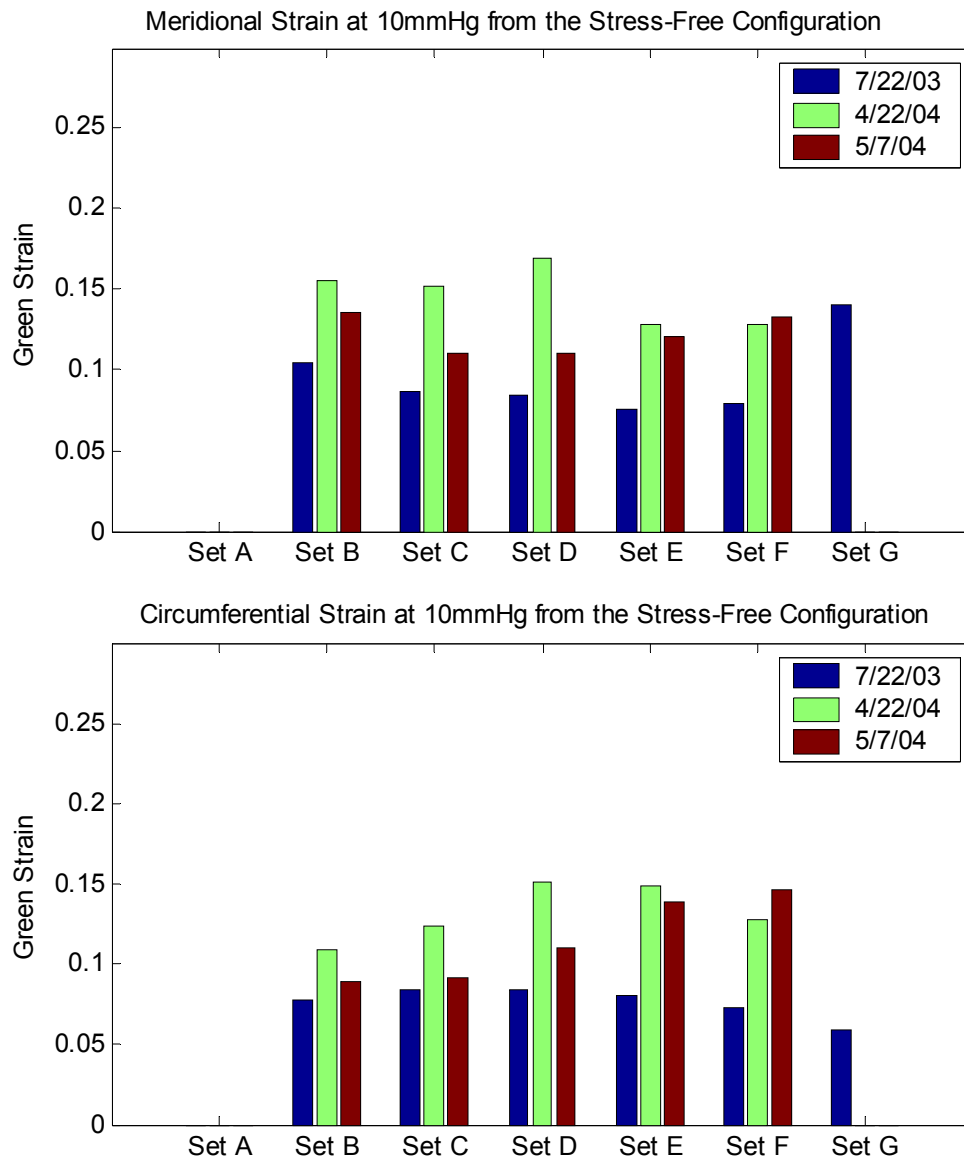


Fig. 19. Measured initial strains (strains at 10 mmHg with respect to the stress-free configuration) by region. Note that markers are often lost near the equator when cutting the anterior lens capsule free for this measurement.

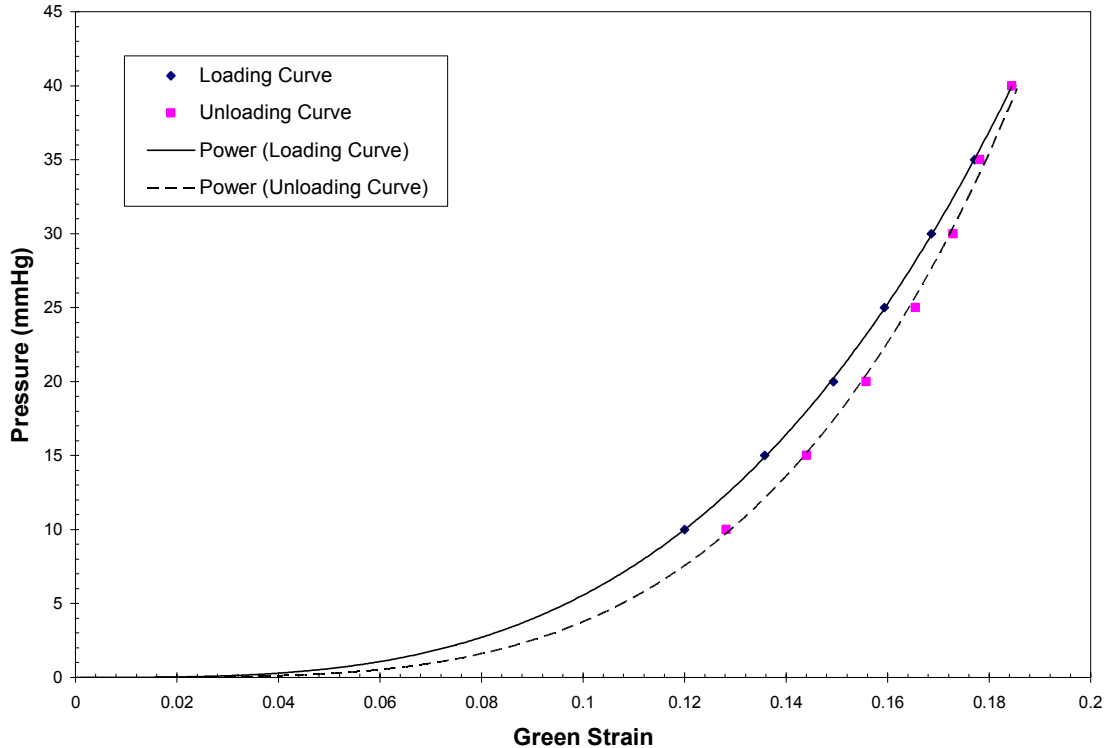


Fig. 20. Average loading and unloading data from set D of six experiments, shown with power curve of the form $y = Ax^b$, predicting strain values at pressure states that could not accurately be measured. Note the high nonlinearity of the curve.

Discussion

Despite its fundamental importance in physiologic processes such as accommodation and clinical interventions such as cataract surgery, our understanding of the mechanical behavior of the lens capsule remains incomplete. Early work by Fisher (1969a) suggested that the ultimate tensile stress of the human anterior lens capsule decreases with age from 2.3 MPa to 0.7 MPa, yet these results are limited by both the experimental set-up and the method of data analysis. Data were collected via pressure-volume tests, which are essentially 1-D and averaged over multiple regions and

directions, and data were reduced using a result from linearized elasticity. The latter is inappropriate given the nonlinear material behavior and finite strains.

There are also data from various “unconventional” mechanical tests. For example, Krag et al. (1993) measured the pressure required to express the lens following a continuous circular capsulorhexis (CCC). They found that the posterior lens capsule ruptures at 59 ± 10 mmHg, whereas effective “hydroexpression of the lens” required pressures from 3 to 47 mmHg (lower pressures for larger CCCs). Yang et al. (1998) measured the force required for a 0.455 mm diameter rod to puncture the lens capsule when applied normal to the surface. They found that the force required for penetration was significantly higher in the anterior than the posterior lens capsule (9.02 g versus 4.42 g).

Most recently, Krag and colleagues reported many important findings on the uniaxial mechanical and thermomechanical behavior of the porcine and human lens capsule (Krag et al., 1997a, 1998; Krag and Andreassen, 2003). Briefly, they tested intact, circumferential rings of lens capsule in uniaxial tension. Data revealed a highly nonlinear stress-strain relation, with stresses on the order of 4-5 MPa at stretches of 60-80% (1st Piola-Kirchhoff stress versus linearized strain), with no statistically significant difference in behavior between the left and right eye from the same donor. Moreover, despite marked differences in thickness, they found the stress-strain behavior to be the same for the anterior and the posterior capsule. Finally, it was found that mechanical strength and distensibility decrease with age while thickness and stiffness increase with age. These are important findings. Bailey et al. (1993) similarly reported uniaxial

stress-strain data, although as a function of the degree of glycation cross-linking due to incubating porcine lens capsules in a 133 mM glucose solution. As expected, the data reveal that the lens capsule becomes stiffer and less extensible with increasing cross-links, which likely reflects that which occurs in diabetes and aging.

Although uniaxial data provide important insight into some characteristics of the behavior of a material, they are not sufficient for delineating the multiaxial behavior that exists *in vivo*. There is, therefore, a pressing need for multiaxial data. Moreover, it is often preferable to test biological tissues while maintaining their native geometry and mimicking native loading conditions. This is often complicated by the presence of adherent tissue, however, which is why many tissues are excised for testing. We developed a new technique whereby the lens capsule can be isolated from the underlying lens, loaded by in-plane stresses, and yet maintained in nearly its native geometry, with natural boundary conditions around the periphery. Consistent with uniaxial findings, we observed a nonlinear material behavior over finite strains. Furthermore, we found that the strain in the lens capsule varies with region and direction. The meridional strain always appeared to be equal to or greater than the circumferential strain, where their difference was most notable near the equator. These results are not unexpected; indeed, they are qualitatively similar to results obtained for other nonlinear biological membranes such as intracranial saccular aneurysms (Humphrey, 2002).

CHAPTER IV

STRAIN REDISTRIBUTION FROM CAPSULORHEXIS

There are typically three basic steps in cataract surgery. The first step is either a capsulotomy or a capsulorhexis, whereby a central part of the anterior lens capsule is removed so that the clouded lens can be accessed. The second step entails a process called phacoemulsification, in which ultrasound is used to break the clouded lens into pieces that are then aspirated through the hole created by the capsulotomy. The third step involves the skillful insertion of a synthetic material or prosthetic device into the capsular bag to restore focus and thus sight. All three of these steps require extensive manipulation of the lens capsule, which in turn alter the native stress and strain fields. Of these three steps, our focus will be on the redistribution of strain and changes in curvature due to the anterior capsulotomy.

The most common technique for gaining access to the lens is the creation of a continuous circular capsulorhexis (CCC), in which a circular tear is made via a continuous circumferential tearing of the lens capsule. This method is preferred because it provides a strong circular edge, resistant to radial tearing during insertion of the IOL. In addition, this technique allows for the creation of a smaller diameter hole, which has been shown by Hollick et al. (1999) to decrease the occurrence of PCO.

Because the lens capsule is thin-walled with a large radius of curvature, it may be treated mechanically as a membrane, which in turn implies that curvatures influence greatly the local stress field. Herein, we report measurements of the changes in in-plane

finite strain and curvature in the anterior lens capsule of porcine eyes following a continuous circular capsulorhexis performed by an experienced veterinary ophthalmologist.

Experimental Methods

Our basic experimental procedures and test system are similar to those discussed in Chapter III. Briefly, we mount fresh, enucleated eyes in a moldable wax fixture, remove the cornea and iris, and then affix numerous (40 - 50) closely placed, 40 μm diameter fluorescent microspheres to the surface of the anterior lens capsule. After immersing the eye in a physiologic solution (Alcon BSS) and warming it to 35°C, we then use blue light to excite the markers and a bi-plane video system (current resolution of $\sim 7 \mu\text{m}$) to monitor their 3D positions both before and after a continuous circular capsulorhexis.

Analysis

Strain Calculation

Global reconstruction techniques can then be used with the biplane video system to determine the 3D position of the centroid of each marker as detailed in the 3D Object Reconstruction part of the Analysis section in Chapter III. Once the 3D Cartesian coordinates of each marker are known, a Delaunay triangularization technique (Matlab) is used to construct an array of lines connecting marker centroids, thus forming a triangular mesh over the entire field of markers, with nodes at each marker centroid. The triangles are of similar size and shape so that the corners of each triangle form a marker triplet, appropriate for measuring strain.

Regional, in-plane components of Green strain can then be calculated from the motions of these closely spaced marker triplets as described previously in the Strain Calculation part of the Analysis section of Chapter III. Briefly, the Green strain, \mathbf{E} , which is exact for finite strains and independent of rigid body rotations, is computed locally for each triplet using the deformation gradient, \mathbf{F} , through the equation $\mathbf{E} = \frac{1}{2}(\mathbf{F}^T \mathbf{F} - \mathbf{I})$. The deformation gradient can be calculated directly for each marker triplet by finding how position vectors before the CCC (denoted by $\Delta \mathbf{X}$ and connecting vertices of the triplets) deform to position vectors after the CCC (denoted by $\Delta \mathbf{x}$). Since the marker triplets are close together and there are no severe deformation gradients, we can assume a homogeneous deformation within each triangular region; thus, $\Delta \mathbf{x} \approx \mathbf{F}(\Delta \mathbf{X})$, which can easily be solved using matrix methods (Humphrey, 2002). The directional components of in-plane strain for each marker triplet are labeled as meridional and circumferential. They are perpendicular to each other and tangent to the lens capsule at the origin of the localized strain region, which is prescribed to be at the centroid of each marker triplet. The meridional direction always points to the anterior pole of the lens capsule, which is defined by the Y-suture (See Fig. 10).

Finally, it is important to note that strains reported herein refer to the in situ, unloaded reference configuration (the native state of the lens capsule), not a stress-free reference configuration. As shown by Delange (2002), the normal lens capsule is under a pre-strain of roughly 8% in the circumferential direction and 13% in the meridional direction. In this chapter, however, we compute only the change in strain from the native state, not absolute strain.

Curvature Calculation

Curvature is a measure of how an outward unit normal vector changes its orientation along a prescribed arc length. Curvature can be found from a variety of methods. One way would be to measure it directly from the 3D coordinates of the markers, using a finite differencing technique for calculation of the derivatives in the curvature equation; however, this would require the computation of second-order derivatives. Therefore, it would be more appropriate to develop a mathematical model of the lens capsule. A good mathematical model must contain the equation for a surface in three-space that closely approximates native lens capsule geometry. If the model is good, it can be used to compute curvatures analytically, and these curvatures should closely approximate those of the native anterior lens capsule.

As a first approach in modeling the anterior lens capsule, we made several simplifications by assuming certain symmetry conditions and geometry constraints. For instance, the eye was placed under the biplane video system such that the transverse plane and the sagittal plane were nearly aligned with the xz plane and yz plane of a laboratory Cartesian coordinate system. Note that these anatomical planes are of importance since it is assumed that the major and minor axes of the anterior lens capsule reside in these planes. Furthermore, the anterior lens capsule appears to be a smooth surface with near constant concavity. Therefore, we looked at various polynomial functions of the form $z = f(x,y)$, which had, at most, second order terms in x and y . These types of functions represent a family of surfaces known as quadrics. The general form of the equation for a quadric is mathematically appealing, since it is linear in terms of the

unknown parameters; thus, these parameters can be found using linear least squares regression. Moreover, the first and second derivatives of the quadric can easily be calculated, and curvature is computed in the x and y directions (major and minor axes of the lens capsule, respectively) from the standard curvature equations

$$\kappa_x = \frac{\left| \frac{\partial^2 z}{\partial x^2} \right|}{\left(1 + \left(\frac{\partial z}{\partial x} \right)^2 \right)^{3/2}} \quad \text{and} \quad \kappa_y = \frac{\left| \frac{\partial^2 z}{\partial y^2} \right|}{\left(1 + \left(\frac{\partial z}{\partial y} \right)^2 \right)^{3/2}}. \quad (5)$$

Although the general form for a quadric provides a reasonable model of the anterior lens capsule, more sophisticated mathematical models were still examined. For instance, we exploited the suggestion that the anterior lens capsule is a hemi-ellipsoid (Fisher, 1969b) and modeled it this way by finding the least squares solution to the algebraic representation of an ellipsoid. As shown by Chatterjee and Chong (1997), an ellipsoid with general orientation can be expressed algebraically as

$$\mathbf{x}^T \bar{\mathbf{A}} \mathbf{x} + \bar{\mathbf{b}}^T \mathbf{x} + \bar{c} = 0 \quad (6)$$

where $\mathbf{x} = [x, y, z]^T$ are the 3D coordinates for each marker, and the symmetric and positive definite matrix $\bar{\mathbf{A}}$, the vector $\bar{\mathbf{b}}$, and the scalar \bar{c} , are given by

$$\bar{\mathbf{A}} = \begin{bmatrix} A & D/2 & E/2 \\ D/2 & B & F/2 \\ E/2 & F/2 & C \end{bmatrix}, \quad \bar{\mathbf{b}} = \begin{bmatrix} G \\ H \\ K \end{bmatrix}, \quad \text{and} \quad \bar{c} = L.$$

This can also be written in the form

$$Ax^2 + By^2 + Cz^2 + Dxy + Exz + Fyz + Gx + Hy + Kz + L = 0, \quad (7)$$

subject to the constraints that $D^2 < 4AB$, $E^2 < 4AC$, and $F^2 < 4BC$, so that $\bar{\mathbf{A}}$ is symmetric and positive definite.

Note that there are ten parameters in Eq. 7, but there should only be nine for a general ellipsoid, because an ellipsoid has nine degrees of freedom. For instance, an ellipsoid can be completely described by its three radii, the displacement of its center from the origin of a laboratory Cartesian coordinate system, and rotations of the ellipsoid about all three axes of the coordinate system. Therefore, it is necessary to either eliminate a parameter or impose some suitable constraint. Turner et al. (1999) examined how the parameters in Eq. 7 relate to the ellipsoid's center, semi-axes, and orientation. They note that A , B , and C are strictly positive and D , E , and F are near zero if the rotations of the ellipsoid about the axes of the coordinate system are small. Furthermore, G , H , and K are near zero for ellipsoids centered near the origin (and in other cases as well) and L is near zero in a number of instances. Observation of the physical constraints imposed by our experimental method reveal that the eye is oriented with our coordinate system in such a way that an ellipsoid modeling the anterior lens capsule should have negligible rotations about the x and y axes. Therefore, the parameters E and F can be eliminated, and the remaining eight parameters can be determined using linear least squares regression with the coordinate data.

The advantage of this ellipsoid-fitting approach is its simplicity, but the disadvantage is that we do not know what we are minimizing in a geometrical sense, when obtaining the linear least squares solution. Additionally, this best "algebraic fit" ellipsoid does not produce the best "geometric fit". In fact, Gander et al. (1994) showed

that the best “algebraic fit” can be a poor estimate of the geometry described by coordinate data. Therefore, we refined our approach by finding the best geometrical-fitting ellipsoid. That is, we solved for the weighted, least-squares, best-fit parameters of an ellipsoid by minimizing the difference between measured and modeled surface positions.

In finding the best “geometric fit” ellipsoid, it is best to use a parametric representation, such as

$$\begin{bmatrix} x \\ y \\ z \end{bmatrix} = \mathbf{R}_1 \mathbf{R}_2 \mathbf{R}_3 \begin{bmatrix} r_1 \cos u \cos v \\ r_2 \sin u \cos v \\ r_3 \sin v \end{bmatrix} + \begin{bmatrix} x_c \\ y_c \\ z_c \end{bmatrix}, \quad (8)$$

where $-\pi \leq u < \pi$ and $-\pi/2 \leq v < \pi/2$ are scalar auxiliary parameters; $[x_c, y_c, z_c]^T$ are coordinates for the origin of the ellipsoid; r_1, r_2 , and r_3 are radii of the axes of the ellipsoid; and $\mathbf{R}_1, \mathbf{R}_2$, and \mathbf{R}_3 are plane rotation matrices given by

$$\mathbf{R}_1 = \begin{bmatrix} \cos \theta_x & \sin \theta_x & 0 \\ -\sin \theta_x & \cos \theta_x & 0 \\ 0 & 0 & 1 \end{bmatrix}, \mathbf{R}_2 = \begin{bmatrix} \cos \theta_y & 0 & \sin \theta_y \\ 0 & 1 & 0 \\ -\sin \theta_y & 0 & \cos \theta_y \end{bmatrix} \text{ and } \mathbf{R}_3 = \begin{bmatrix} 1 & 0 & 0 \\ 0 & \cos \theta_z & \sin \theta_z \\ 0 & -\sin \theta_z & \cos \theta_z \end{bmatrix}.$$

We are interested in minimizing the geometric distances between measured marker positions and the model ellipsoid, where the geometric distance is defined as the distance between a marker and its closest point on the ellipsoid (Gander et al., 1994).

We can solve this optimization problem by finding the values for the parameter set \mathbf{s} that minimizes the quadratic function

$$Q = \sum_{i=1}^N \left[\left(x_i^{[m]} - x(u_i, v_i) \right)^2 + \left(y_i^{[m]} - y(u_i, v_i) \right)^2 + \left(z_i^{[m]} - z(u_i, v_i) \right)^2 \right] \quad (9)$$

for all markers ($i = 1 \dots N$) where the coordinates of the i th marker are $x_i^{[m]}, y_i^{[m]}, z_i^{[m]}$, and the parameter set is $\mathbf{s} = [u_1 \dots u_m, v_1 \dots v_m, r_x, r_y, r_z, x_c, y_c, z_c, \theta_1, \theta_2, \theta_3]^T$. This is a non-linear problem, which must be solved iteratively, as, for example, by using an algorithm such as the Marquardt-Levenberg method.

The biggest difficulty with this approach is that it is hard to generate initial estimates for the parameter set \mathbf{s} . This complication can be overcome, however, by first finding the parameters for the best ‘‘algebraic fit’’ and then relating them to the parameters in \mathbf{s} , so that they can be used as initial parameter estimates, $\hat{\mathbf{s}}$. The relationship between the parameters from the best ‘‘algebraic fit’’ and the parameters in \mathbf{s} can be found by introducing an ellipsoid-oriented Cartesian coordinate system $\hat{\mathbf{x}}$, such that this new coordinate system has its origin at the center of the ellipsoid, and its coordinate directions aligned with the axes of the ellipsoid. The laboratory coordinate system \mathbf{x} , can be related to the rotated and shifted ellipsoid-oriented coordinate system $\hat{\mathbf{x}}$ by the equation

$$\mathbf{x} = \mathbf{Q}\hat{\mathbf{x}} + \mathbf{t}, \quad (10)$$

so that Eq. 6 becomes

$$\hat{\mathbf{x}}^T \hat{\mathbf{A}} \hat{\mathbf{x}} + \hat{\mathbf{b}}^T \hat{\mathbf{x}} + \hat{c} = 0, \quad (11)$$

with

$$\hat{\mathbf{A}} = \mathbf{Q}^T \bar{\mathbf{A}} \mathbf{Q}, \quad \hat{\mathbf{b}}^T = (2\mathbf{t}^T \bar{\mathbf{A}} + \bar{\mathbf{b}}^T) \mathbf{Q}, \quad \text{and} \quad \hat{c} = \mathbf{t}^T \bar{\mathbf{A}} \mathbf{t} + \bar{\mathbf{b}}^T \mathbf{t} + \bar{c}.$$

This coordinate transformation was chosen with specific \mathbf{Q} and \mathbf{t} so that $\hat{\mathbf{b}} = \mathbf{0}$ and $\hat{\mathbf{A}}$ contains the eigenvalues of $\bar{\mathbf{A}}$ (Gander et al., 1994). Therefore, Eq. 11 can be written as

$$\lambda_1 \hat{x}^2 + \lambda_2 \hat{y}^2 + \lambda_3 \hat{z}^2 + \hat{c} = 0, \quad (12)$$

where λ_1, λ_2 and λ_3 are the eigenvalues of $\bar{\mathbf{A}}$, and they must all be positive since $\bar{\mathbf{A}}$ is symmetric and positive definite. Furthermore, the columns of \mathbf{Q} are eigenvectors of $\bar{\mathbf{A}}$ and $\mathbf{t} = -(1/2)\mathbf{A}^{-\text{T}}\mathbf{b}$ so that $\hat{\mathbf{b}} = \mathbf{0}$. Finally, $\hat{\mathbf{s}}$ can be calculated from the known parameters of the best ‘‘algebraic fit’’ ellipsoid using the following equations:

$$\begin{aligned} r_i &= \sqrt{-\hat{c}/\lambda_i}, \\ \mathbf{x}_c &= \mathbf{t}, \\ \mathbf{R}_1 \mathbf{R}_2 \mathbf{R}_3 &= \mathbf{Q}, \end{aligned} \quad (13)$$

for $i = 1, 2, 3$ and $\mathbf{x}_c = [x_c, y_c, z_c]^{\text{T}}$. The set $\hat{\mathbf{s}}$ can then be used in a non-linear least squares regression to find the best-fitting parameter set \mathbf{s} .

Once the parameters of the ellipsoid are known, they can be used in the partial derivatives of Eq. 8, with respect to u and v . These derivatives can then be transformed to the ellipsoid oriented coordinate system $\hat{\mathbf{x}}$, and curvature in the meridional direction can be calculated along the major and minor axes by using the equation

$$\kappa = \frac{|\hat{z}'(v)\hat{w}''(v) - \hat{w}'(v)\hat{z}''(v)|}{\left(\sqrt{\hat{z}'(v)^2 + \hat{w}'(v)^2}\right)^3}, \quad (14)$$

where $u = 0$ and \hat{w} represents \hat{x} for curvature along the major axis and $u = \pi/2$ and \hat{w} represents \hat{y} for curvature along the minor axis.

It is important to note the ellipsoid is oriented in such a way that the section defined parametrically by $-\pi \leq u < \pi$ and $\theta_m \leq v < \pi/2$ models the anterior lens capsule, where θ_m is the elevation angle of the equator of the capsule (see Fig. 21).

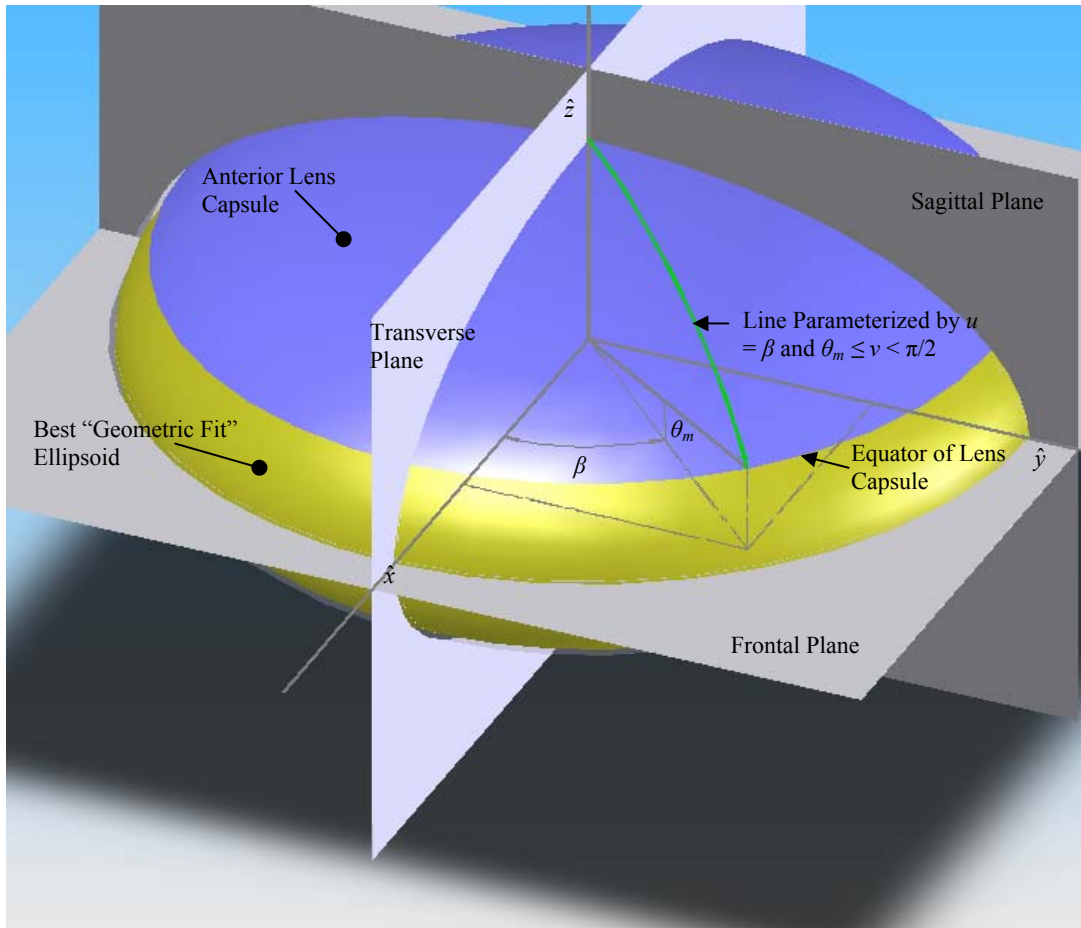


Fig. 21. Drawing that illustrates how the best “geometric fit” ellipsoid models the anterior lens capsule.

If the major diameter, d_m , of the capsule is known, then θ_m can be calculated from geometry as

$$\tan(\theta_m) = \frac{2r_2}{d_m} \left(1 - \frac{d_m^2}{r_1^2} \right)^{\frac{1}{2}}. \quad (15)$$

Once again, we assume that the major and minor axes of the lens capsule reside in the transverse and sagittal planes, respectively. If this conjecture is true, then the anterior lens capsule is aligned with the ellipsoid such that the $\hat{x}\hat{z}$ plane is the transverse plane,

and the $\hat{y}\hat{z}$ plane is the sagittal plane (as shown in Fig. 21). Furthermore, the two curves on the ellipsoid, parameterized by $u = 0$ (in the $\hat{x}\hat{z}$ plane) and $u = \pi/2$ (in the $\hat{y}\hat{z}$ plane) with $\theta_m \leq v < \pi/2$ represent the surface of the lens capsule along the major and minor axes, respectively.

We are most interested in the principal curvatures along these axes. One principal curvature can be found by using the derivatives of Eq. 8 in Eq. 14 for $u = 0$ and $u = \pi/2$. This principal curvature describes how the unit outward normal changes with arclength along the parametric curves representing the major and minor axes of the capsule. The other principle curvature can be found from the first principle curvature using differential geometry.

Results

Fig. 22 is a picture of the anterior surface of the lens capsule immediately following a continuous circular capsulorhexis, with a diameter of 5 mm, centered at the Y-suture of the lens. Although only partially visible in normal lighting, the 40- μm diameter fluorescent microspheres can be seen as the small white dots in the upper-right quadrant. Fig. 23 is an image from the biplane video system, showing a portion of the marker field remaining after the CCC; the microspheres have been excited with blue light. Note the high image quality and excellent contrast obtained with the biplane video system.

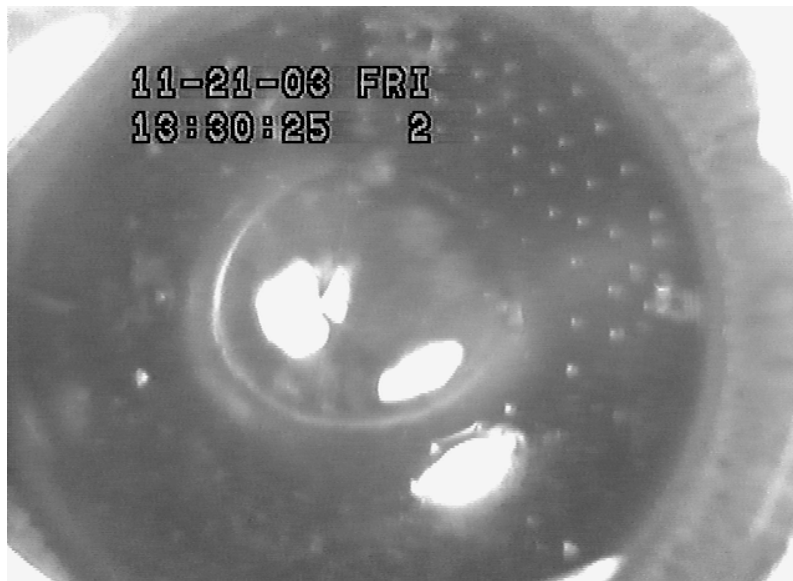


Fig. 22. Anterior Lens Capsule with field of markers in top-right quadrant immediately after surgical introduction of CCC with 5 mm diameter. Note that this picture was imaged with a separate video system and VCR, not the experimental biplane video system, which provides better resolution and more contrast, as seen in Fig. 23.

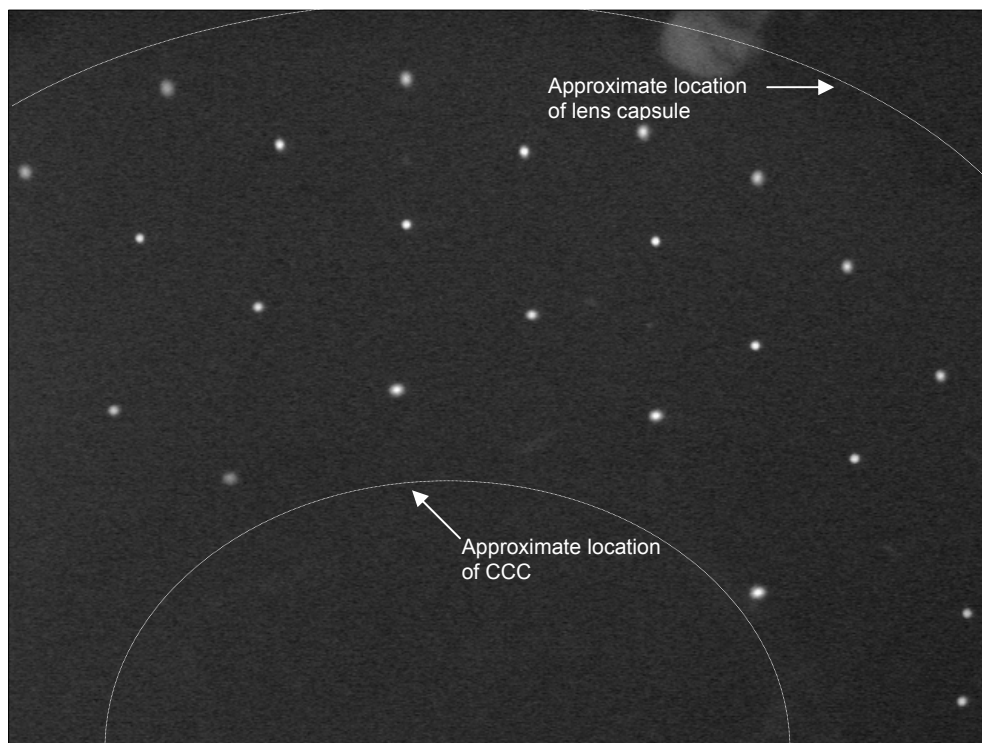


Fig. 23. Section of anterior lens capsule imaged with the experimental biplane video system; shown is a portion of marker field remaining after a CCC.

Fig. 24 to Fig. 28 show the meridional and circumferential strain fields in a quadrant of the anterior lens capsule resulting from a CCC, approximately 5 mm in diameter, for five different specimens. For visual purposes, the strain fields were each plotted on an ellipsoid surface that represents the overall dimensions (in millimeters) of a typical, porcine anterior lens capsule. The x -direction is oriented along the transverse plane while the y -direction is oriented along the sagittal plane. The strain range for each figure is chosen between limits set by the minimum meridional strain and the maximum circumferential strain calculated for that particular specimen. It is evident from the figures that a high degree of strain redistribution occurs as a result of the CCC. We found that strain increases up to 20% in the circumferential direction and decreases nearly 20% in the meridional direction, each relative to the in situ reference configuration. Furthermore, the magnitude of strain was always greater near the edge of the CCC and almost zero near the equator. Both directional components of strain also appear slightly greater along the transverse plane than the sagittal plane.

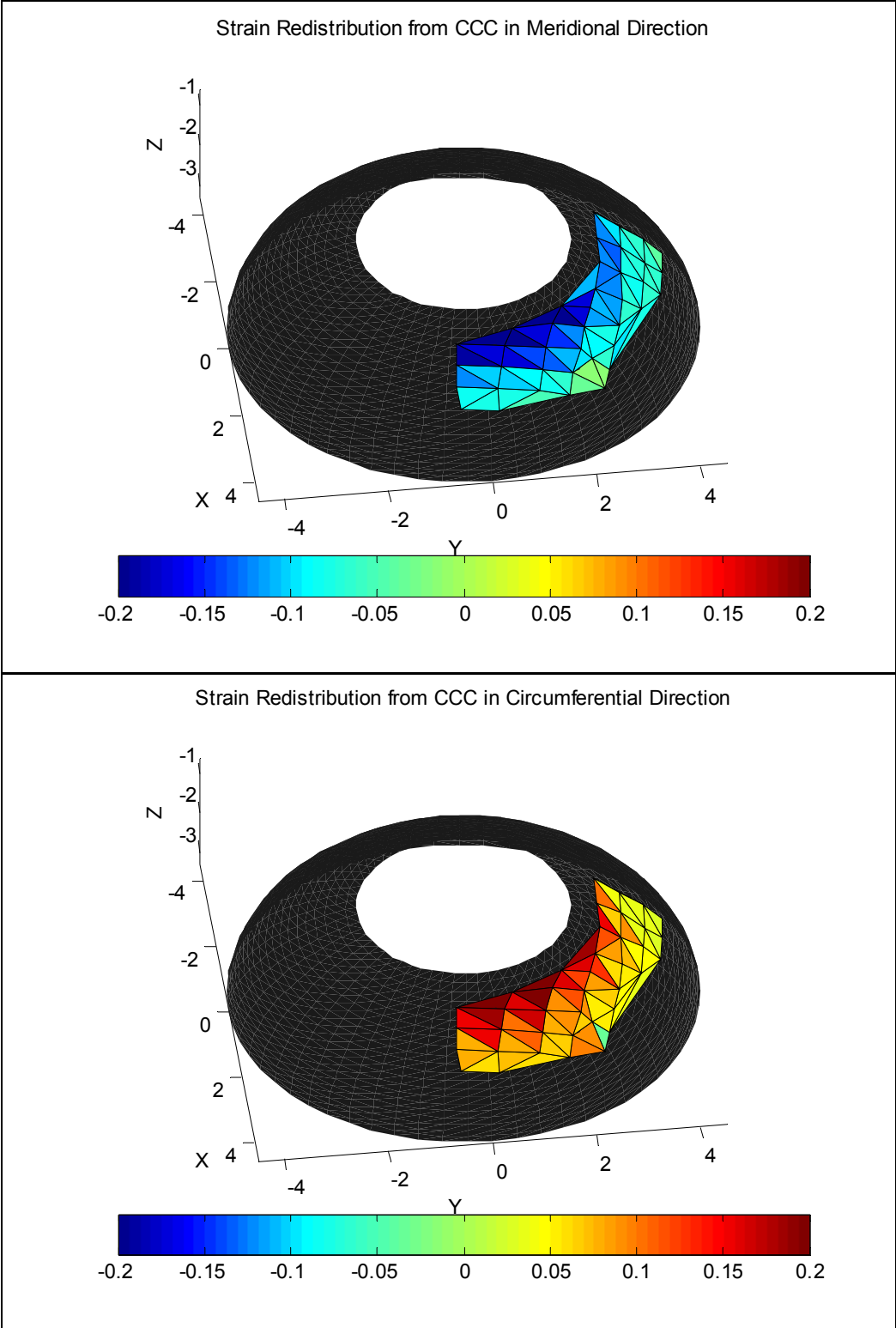


Fig. 24. Strain field in top-right quadrant of anterior lens capsule after introduction of CCC with 5 mm diameter. (Specimen: 1, Number of nodes: 39, Number of elements: 59)

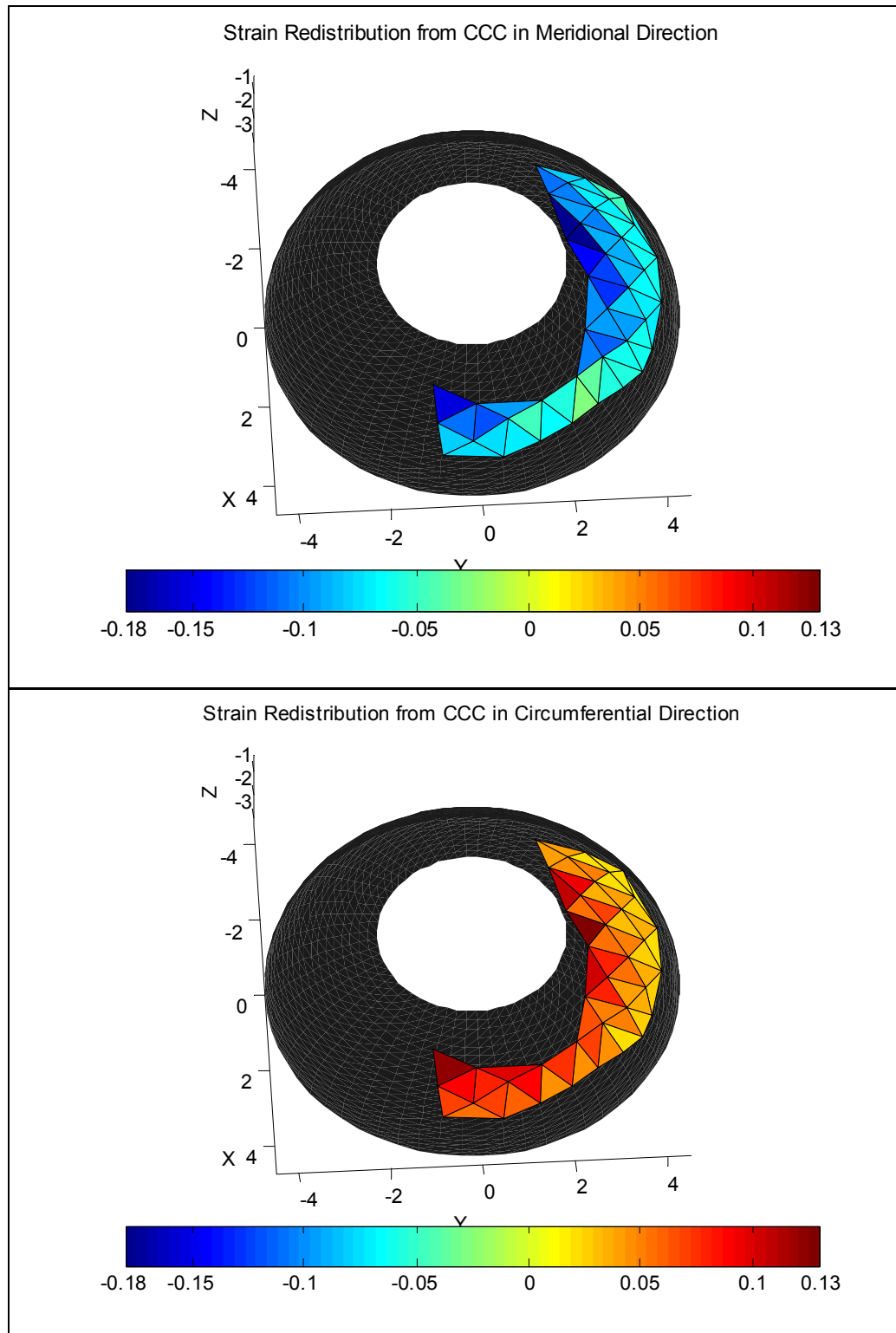


Fig. 25. Strain field in top-right quadrant of anterior lens capsule after introduction of CCC with 5 mm diameter. (Specimen 2, Number of nodes: 38, Number of elements: 50)

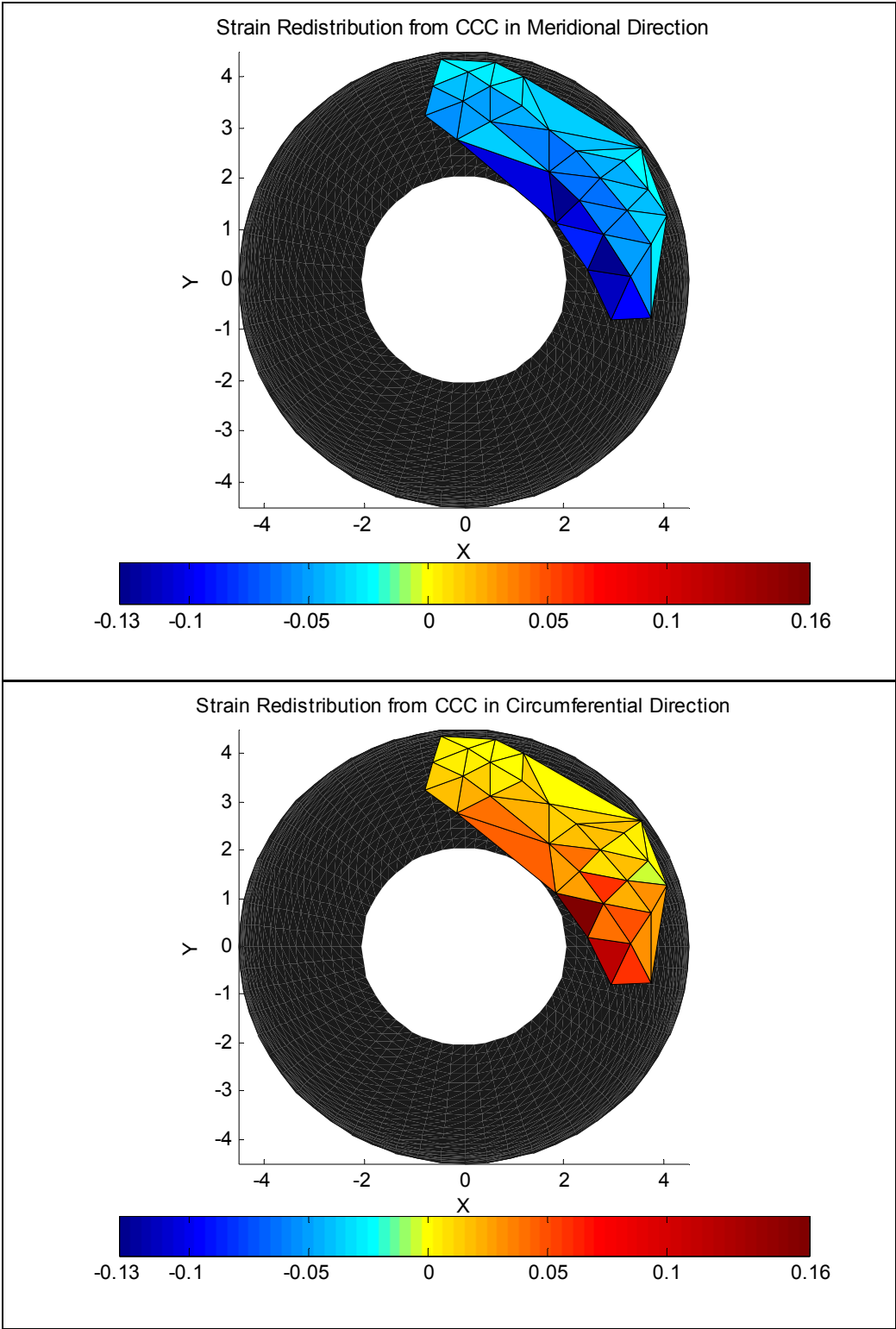


Fig. 26. Strain field in top-right quadrant of anterior lens capsule after introduction of CCC with 4.5 mm diameter. (Specimen 3, Number of nodes: 28, Number of elements: 42)

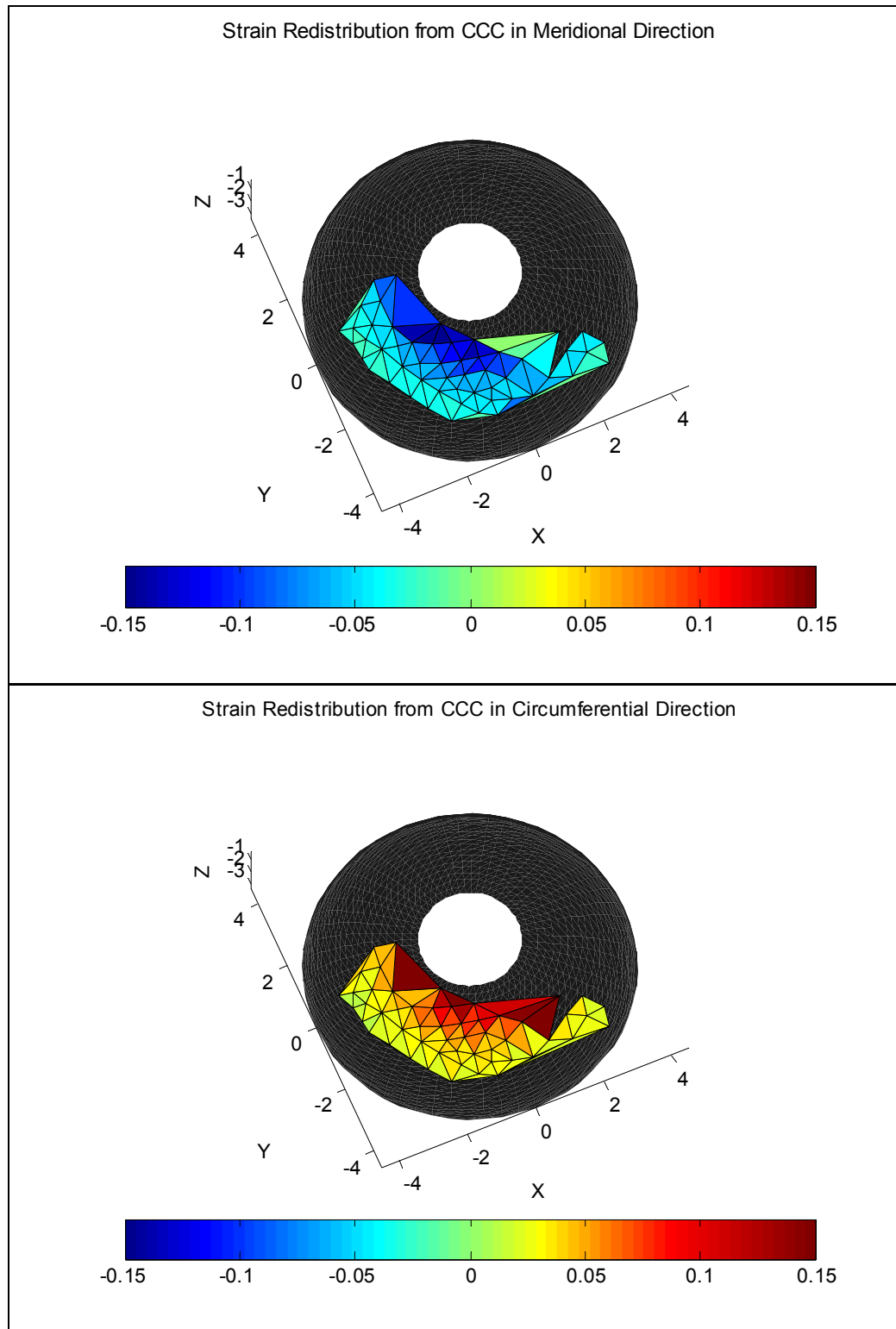


Fig. 27. Strain field in top-right quadrant of anterior lens capsule after introduction of CCC with 3.5 mm diameter. (Specimen 4, Number of nodes: 53, Number of elements: 85)

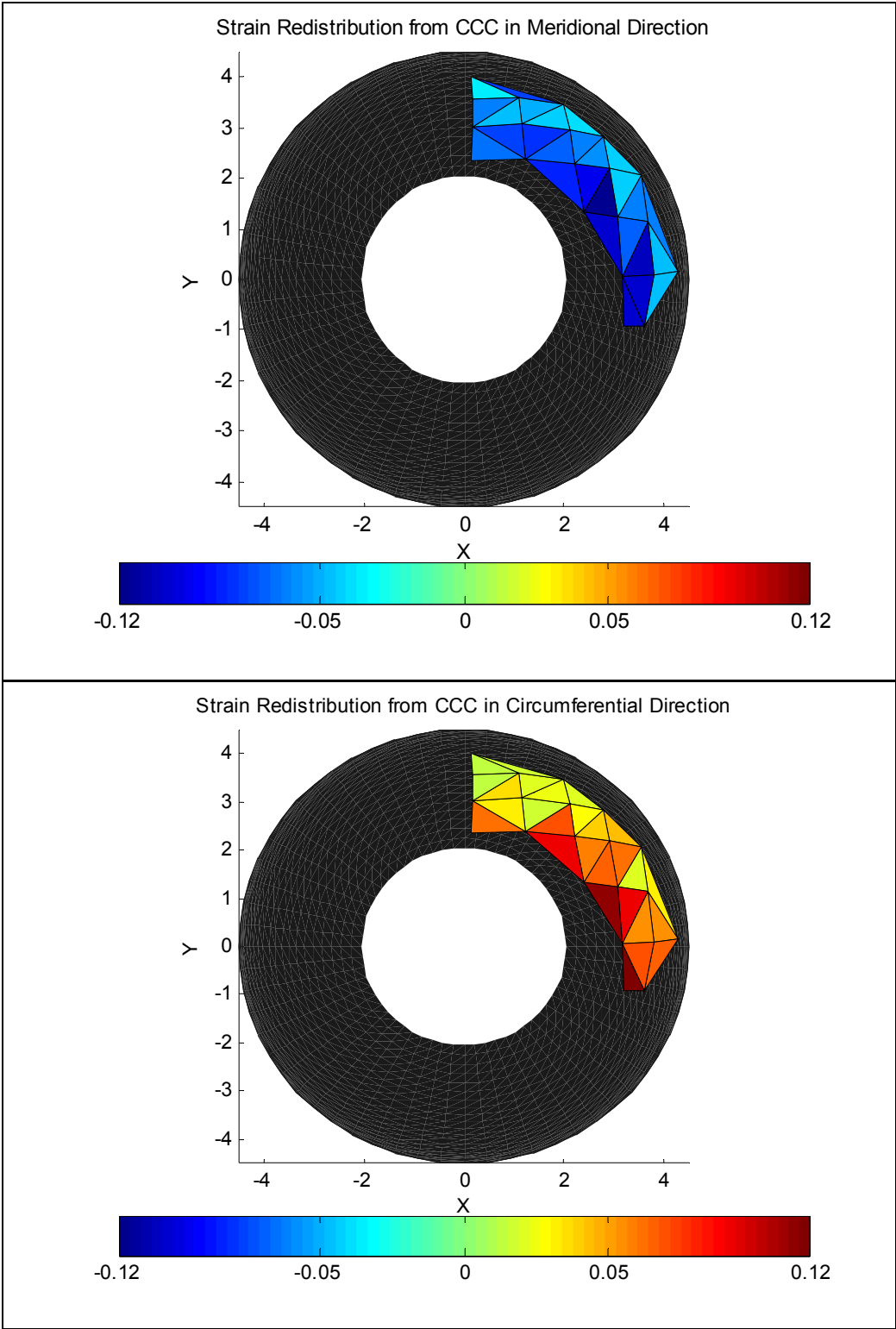


Fig. 28. Strain field in top-right quadrant of anterior lens capsule after introduction of CCC with 4 mm. diameter. (Specimen 5, Number of nodes: 21, Number of elements: 27)

Fig. 29 is a plot of a quadric surface fit to the marker coordinates of specimen 5 before the CCC (using TableCurve 3D); the equation of the quadric is shown along with associated parameter values. Unfortunately, the parameters have no physical meaning, and the equation is not written in parametric form. Nevertheless, we can still calculate curvature analytically, along the x and y directions using the equations for κ_x and κ_y given in Eq. 5. Fig. 30 is a plot of the inverse curvature in the x and y direction of the quadric, which is an approximation of curvature in the major and minor axes of the anterior lens capsule, both before and after the CCC. The abscissa represents the distance along the meridional direction from the anterior pole to the equator.

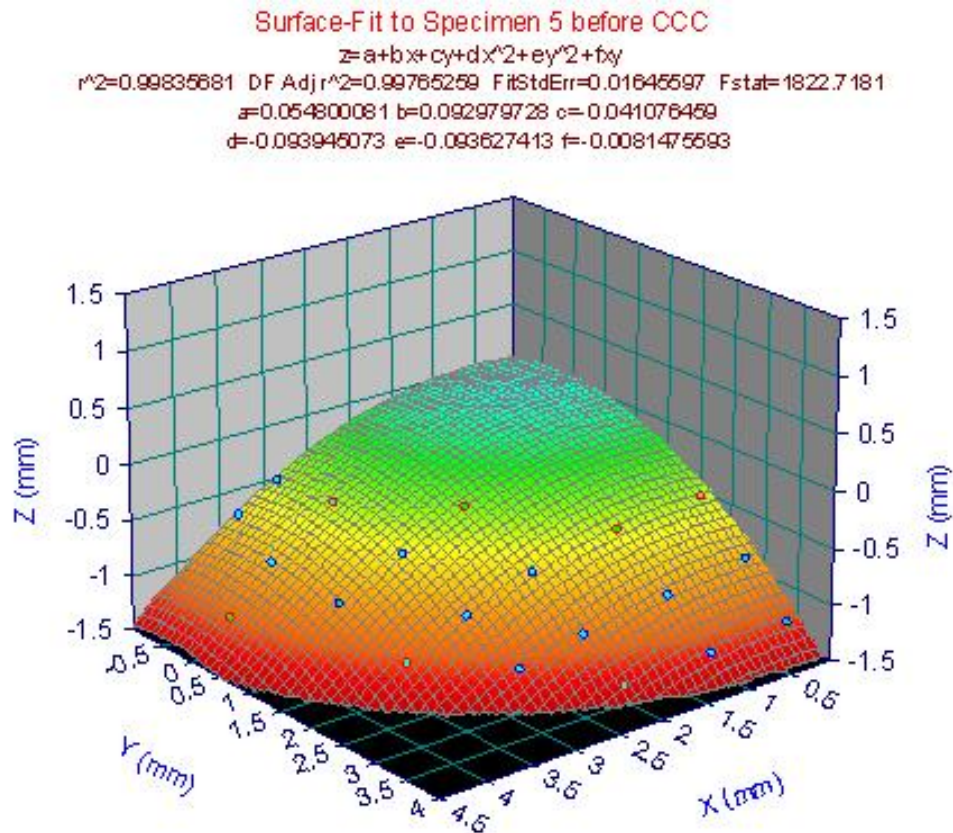


Fig. 29. Plot showing section of a quadric fit to marker coordinates before CCC (using TableCurve 3D).

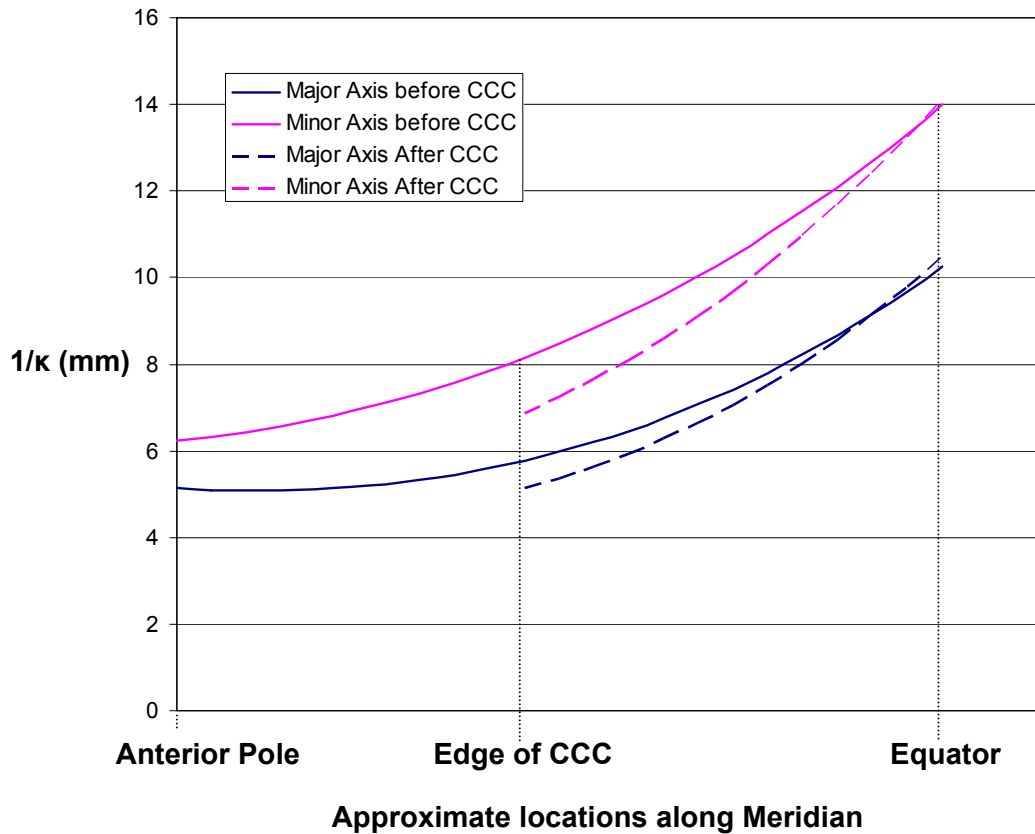


Fig. 30. Estimates of the curvature along the major and minor axes of the anterior lens capsule, both before and after the CCC.

Discussion

The normal lens capsule consists primarily of type IV collagen, with admixed adhesion molecules and proteoglycans, woven in a fine 3D network structure having polygonal-shaped interstices ~ 20 nm in diameter (Barnard et al., 1992). Given the thin-wall (on the order of $30 \mu\text{m}$ for the human anterior lens capsule) and large radius of curvature (~ 7 mm), these observations justify the use of a membrane assumption within a framework of continuum mechanics. It is well known in mechanics that introducing a hole in a material under load usually results in highly non-uniform stress and strain

fields, including marked stress concentrations at the edge of the hole. Recently, however, we showed that the degree of material anisotropy (e.g., a circumferentially versus radially stiffer behavior) can dramatically affect the stress and strain distributions around a hole in a flat, pre-stressed, nonlinear membrane subjected to finite strains (David and Humphrey, 2004). Given the lack of a similar solution for a distended ellipsoidal membrane, there was a need for experimental measurements of the changes in strain and curvatures in the lens capsule following a CCC.

As expected, we found considerable redistribution of strain from the CCC in all specimens. The results seem reasonable from a mechanics point of view, as evident from the relatively smooth strain gradients and decreasing magnitude of strain from the CCC edge to the equator. Moreover, negative strains in the meridional direction (consistent with a retraction) and positive strains in the circumferential direction (consistent with an increase in fictitious circumferences) are both consistent with the concept of pre-strain in the lens capsule (i.e. the lens capsule is stretched in its in-situ state, thus the introduction of a tear or cut will cause retraction of the capsule).

It also appears that the CCC causes slight changes in curvature; this is expected in part because the CCC creates a traction-free boundary condition at the edge of the tear. In addition, this suggests that the CCC allows the lens to change shape, perhaps tending to bulge-out near the edge of the CCC. Regardless, curvature should change most notably at the edge and should remain nearly the same close to the equator (as evident in Fig. 30). Note, too, that Gauss-Codazzi relations combined with equilibrium equations from membrane theory reveal that the meridional stress resultant is inversely

related to the second principal curvature. Thus, as stress decreases in the meridional direction, after the CCC, curvature is expected to increase, thus qualitatively validating our curvature results.

Although the curvatures seem reasonable, there is a need to parameterize the surface more rigorously and to calculate principal curvatures along the major and minor axes. This, along with equations derived from membrane theory, will allow us to calculate regional stress resultants in the lens capsule and quantify their changes as a consequence of the CCC. Furthermore, if thickness of the lens capsule is measured as a function of arclength, then the regional stress resultants can be divided by localized thickness measurements to calculate the stress field over the entire lens capsule.

CHAPTER V

DISCUSSION

The functionality of our testing system and repeatability of our experimental methods have been validated by the consistency of our data and the successful duplication of experiments performed by Delange (2002). Furthermore, we have been able to explain some of the variability seen in the pressure-strain data and pre-strain data reported by Delange (i.e. preconditioning effects and unknown lens interactions at pressures below 10 mmHg). Not only have we reproduced previous data, but we have added new, important information, such as accurate 3D geometry of the lens capsule, preconditioning studies, and strain redistribution due to CCC.

In review, two different sets of experiments were conducted: multiple cycle inflation tests and strain redistribution experiments from the CCC technique. The inflation tests were used to determine the multi-axial mechanical behavior of the porcine lens capsule. This behavior was quantified via pressure-strain data found from the differences between 3D coordinates of markers at various pressure states (note that the 3D coordinates from these tests can also be used to determine the material parameters as discussed in the Calculation of Material Properties section of Chapter VI). Pressure-strain data shows that the porcine anterior lens capsule does indeed exhibit highly nonlinear, pseudoelastic behavior. Strain in the meridional and circumferential direction appears to be nearly the same, except for regions very near the equator, in which case the meridional strains are slightly higher. This increased extensibility in the meridional

direction may be related to differences in geometry (thickness) or material properties (anisotropy), or it may just be a consequence of the displacement boundary condition imposed by the zonules at the equator of the lens capsule. Nevertheless, total strains at 40 mmHg, taken with respect to the stress-free reference configuration, appear to be roughly 18% to 19%. The strain redistribution test showed that strain appears to equally redistribute from the meridional direction to the circumferential direction (i.e. the magnitude of decrease in meridional strain equals the magnitude of increase in circumferential strain). The strain redistribution was highest near the edge of the CCC, reaching magnitudes of 20%. More importantly, the mere existence of strain redistribution verifies the reality of a pre-strain in the lens capsule. These tests also show that introduction of the CCC results in a decreased radius of curvature at the edge of the CCC and almost no change in curvature near the equator, as expected. The significance of these results is most evident when considering how the changes in curvature of the lens capsule affect the changes in curvature of the underlying lens, thus affecting its optical properties. Therefore, the effects of a hole in the lens capsule must carefully be considered in the design of accommodative intraocular lenses. Furthermore, changes in the curvature of the lens capsule are indicative of changes in the stress field present. This can be shown quantitatively by equations derived from membrane theory (as discussed in the Calculating Stress Resultants section of Chapter VI).

The research documented here is only a small part of the ongoing effort to investigate the details of lens capsule behavior, its mechanical properties, and its role in secondary cataracts, as well as its interactions with the lens and zonules in the

accommodative process. The project organization is illustrated in the flowchart from Fig. 31. The darker boxes represent the areas of this project that are still in progress. Recommendations as to why and how these remaining tasks should be completed are discussed in Chapter VI; this includes discussion on the significance of each task, as well as the theoretical framework and methods necessary to complete them.

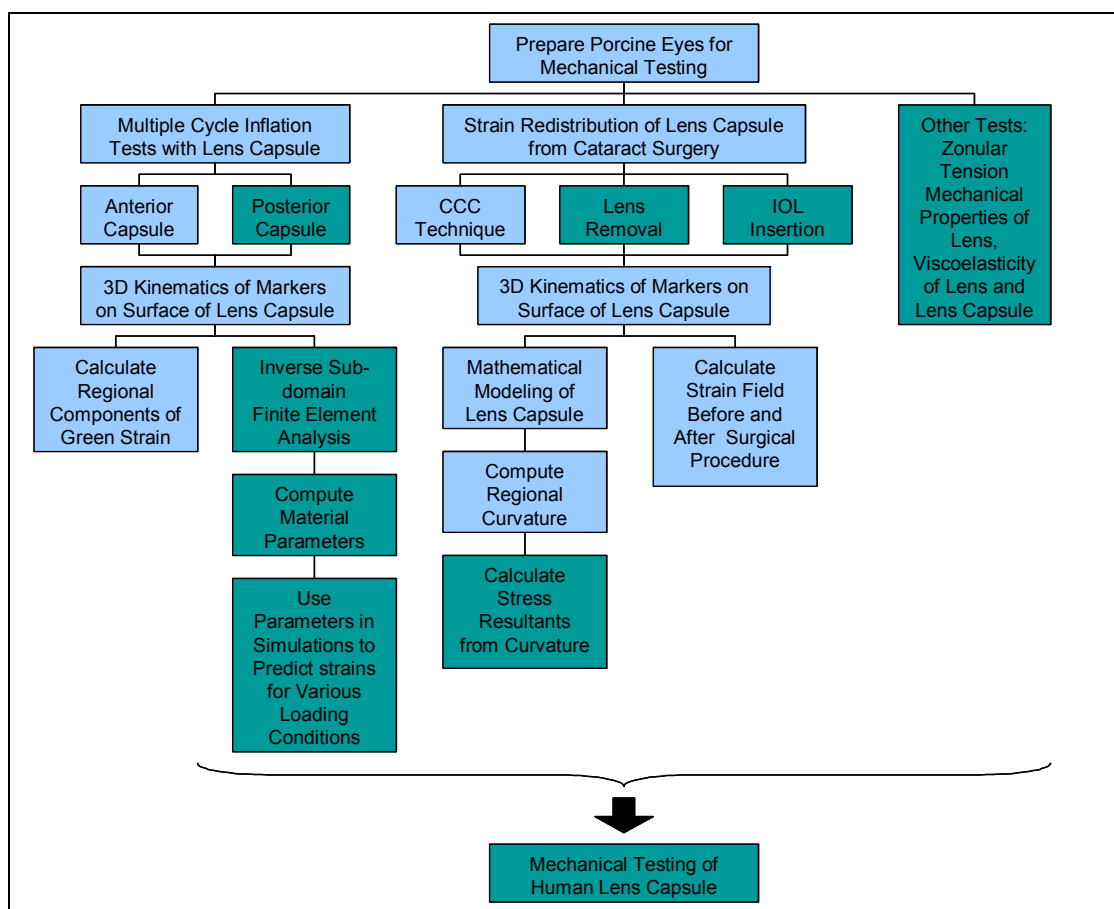


Fig. 31. Flowchart showing project organization. Light boxes indicate work that has been completed, and dark boxes indicate tasks that remain.

Although there is still work to be done, the experimental results presented in this thesis are of great importance since they provide the information necessary to complete

the remaining tasks. For instance, the 3D coordinates from the multiple cycle inflation tests can be used to calculate material properties. Knowledge of the material properties will then allow us to predict the strain response for various loading conditions. This will take us beyond our current experimental capabilities, in that we can run a vast array of simulations for different loading conditions to determine the strain response much faster and more easily than what could be achieved experimentally. Furthermore, the 3D coordinates from the strain redistribution tests can be used in the pursuit of developing better mathematical models for the lens capsule. This will ultimately provide us with better regional curvature measurements necessary for quantifying the stress field in the lens capsule and changes in the stress field that result from various surgical interventions.

CHAPTER VI

RECOMMENDATIONS

Calculation of Material Properties

A large task that remains is quantification of the material properties of the lens capsule. If we treat the inflation of the capsule as a pure mechanics problem, we can use the “inverse approach” to determine the material properties, once the geometry and loading conditions are known. The geometry is found from the 3D coordinates, but the loading conditions are too difficult to determine on the lens capsule as a whole, so we will look at each set of five markers individually. This simplifies the problem since we can consider each set of markers as a displacement boundary value problem, where the displacement of the four corner markers can be measured at each pressurized state. Furthermore, this gives us the advantage of examining heterogeneities by allowing us to quantify different material properties from region to region throughout the lens capsule.

To accomplish this region-by-region analysis, we will employ a sub-domain inverse finite element method to determine the best-fit material parameters, using a constitutive framework, appropriate for nonlinear, pseudoelastic, biological membranes. Therefore, we will use a 2-D Fung-exponential constitutive relation. The material properties will be quantified via a Fung pseudostrain-energy function w ,

$$w = c(e^Q - 1), \quad Q = c_1 E_{11}^2 + c_2 E_{22}^2 + 2c_3 E_{11} E_{22}, \quad (16)$$

where E_{11} and E_{22} are the measured, principal Green strains, and c and c_i ($i = 1,2,3$) are the best-fit material parameters which will be determined. This functional form is chosen based on what is already known about the behavior of the lens capsule, specifically its display of nonlinear elasticity and anisotropy. Furthermore, it has been shown to describe well the data for many soft tissues (Fung, 1993; Humphrey, 2002).

The associated constitutive equation is given by

$$T_{ab} = \frac{1}{\det \mathbf{F}} F_{aC} F_{bD} \frac{\partial w}{\partial E_{CD}}, \quad (17)$$

where T_{ab} are components of the stress resultant tensor \mathbf{T} ($a,b,C,D=1,2$).

The finite element code will use a nonlinear regression algorithm (Marquardt-Levenberg) to determine the set of parameters in the constitutive relation which produces the best match between the computed and measured displacements (at multiple pressures) of the inner node. This can be done by minimizing the objective function e (i.e., $\partial e / \partial c = 0$ and $\partial e / \partial c_i = 0$), where e is given by,

$$e = \sum_{j=1}^m \left[(x_{1|t} - x_{1|e})^2 + (x_{2|t} - x_{2|e})^2 + (x_{3|t} - x_{3|e})^2 \right]. \quad (18)$$

The (x_1, x_2, x_3) denote the Cartesian coordinates of the inner node (marker) at each pressure state j , and subscripts t and e denote finite element-calculated and experimentally-measured, respectively.

Seshaiyer et al. (2001) showed the effectiveness of this finite element method in quantifying the behavior of non-axisymmetric membranes. Many biological tissues can be modeled as membranes, such as aneurysms, skin, and the urinary bladder. For an element to be classified as a membrane, the thickness of the element must be small in

comparison to its in-plane dimensions, the bending stiffness of the element is generally negligible, and the in-plane stresses are assumed to be constant through the thickness.

The lens capsule has been shown by Vaughn et al. (1995) to be classified as a thin-walled structure exhibiting these characteristics. Therefore, the anterior lens capsule can be modeled as a membrane so that the proposed finite element method should be suitable for determining its material properties.

Study of Posterior Capsule

The posterior capsule is thinner and more curved than the anterior lens capsule; it is also devoid of epithelial cells. These characteristic dissimilarities between the posterior and anterior lens capsule, combined with the mechanical differences reported in literature, indicate that the material properties of the posterior lens capsule may be different; thus, it is necessary to study the posterior capsule in addition to the anterior capsule.

The mechanical properties of the posterior lens capsule can be determined using the method discussed in the preceding section. This can only be done once the 3D coordinates of its surface are found at different pressure states from multiple cycle inflation tests. These coordinates can be found using the biplane video system with the same experimental procedure detailed in Chapter III. The only difference is that the posterior half of the eye and the vitreous are removed instead of the cornea.

Mathematical Modeling of Lens Capsule

We attempted to model the anterior lens capsule as part of an ellipsoid, but the nonlinear parameters associated with the best “geometric fit” ellipsoid proved difficult to

solve. The main problem is that the geometry of the anterior lens capsule closely resembles that of an oblate spheroid, in which two of the axes have nearly the same dimension. This can lead to numerical difficulties that often arise when fitting an ellipsoid to near-spherical data. Thus, it may be beneficial to use the technique developed by Turner et al. (1999) to avoid this problem; they derived an alternative parameterization for a best-fitting ellipsoid (in a geometrical, least-squares sense), and iteratively solved for the new parameter set \mathbf{s}^* using a nonlinear least squares method.

It is also possible that higher order terms should be added in the mathematical model of the lens capsule, or on the other hand, it may be better to develop multiple, individual models of different sections of the lens capsule, instead of searching for a global, mathematical representation. For instance, biquadric surface patches have been used for modeling in vivo 3D surface geometry of abdominal aortic aneurysms (AAA) and the right ventricular free wall (Sacks et al., 1993; Sacks et al., 1999). These surface patches use regional parameterization functions of the form

$$S(u, v) = au^2 + 2buv + cv^2, \quad (19)$$

where a local u - v tangent plane coordinate system is used, and the parameters a , b , and c are found for each surface patch by fitting this function to a five by five node grid, digitally reconstructed from images of the specimen surface using MRI.

Since the lens capsule is a smooth surface, we should not encounter the difficulties reported by Sacks et al. (1999), in which the tortuosity of the AAA and the MRI noise required them to use surface smoothing techniques. Furthermore, the smoothness of the lens capsule allows us to use a variety of other mathematical models

as well. Nevertheless, regardless of which method is chosen, the goal of mathematical modeling is measuring curvature of the lens capsule and changes in curvature that result from surgical intervention and accommodation.

Computing Regional Curvatures

Curvature in the lens capsule is important for two reasons. First, it dictates the focal characteristics of the underlying lens substance. Hence, it is necessary to measure regional curvatures as well as changes in curvature that result from surgical intervention, specifically the introduction of a Continuous Circular Capsulorhexis. This information could be very useful in the development of an accommodative IOL. Second, principal curvatures can be used in equations derived from membrane theory to calculate stress resultants in the lens capsule.

Calculating Stress Resultants

In special cases, membrane theory also allows us to calculate stress resultants solely from known loads and geometry, without the explicit specification of a constitutive relation. If the lens capsule is axisymmetric, then the analysis by Humphrey (2002) can be used to write the governing equations for the stress resultants as,

$$T_1 = \frac{P}{2\kappa_2}, \quad T_2 = \frac{P}{\kappa_2} \left(1 - \frac{\kappa_1}{2\kappa_2} \right), \quad (20)$$

where P is the pressure-like traction, exerted on the lens capsule (by either the lens or the inflation pressure if the pressure is high enough to cause separation between the lens and lens capsule) and κ_1 and κ_2 represent the principal curvatures, which can easily be calculated from the mathematical model of the lens capsule. Thus, regional stress

resultants can be measured at any localized region on the lens capsule. Furthermore, if thickness is known as a function of its location, stress can then be calculated from the stress resultants. Therefore, the stress field over the entire lens capsule can be measured, and stress redistribution due to the CCC can be determined if curvature changes are known.

Strain Redistribution from IOL

The strain redistribution due to the Continuous Circular Capsulorhexis (CCC) only provides partial insight into the total changes that occur in the strain field of the lens capsule as a result of cataract surgery. This is mainly because the CCC is only the first of several steps in this surgery. Of most importance, however, is the total strain redistribution which occurs as an end-result of the cataract surgery. In other words, we are most interested in comparing the strain field of the capsule after the intraocular lens (IOL) is inserted with the strain field of the capsule in its native state. Clinically, this comparison will be the most significant, because it shows how the strain redistributes as a result of cataract surgery, and it is this redistribution that we believe alters epithelial function, thus increasing the occurrence of PCO.

The same experimental system and methods discussed in Chapter IV can be used to measure this strain redistribution. The surgery will be modified to include common procedures for cataract extraction (such as phacoemulsification) and insertion of the IOL. Furthermore, it may be of interest to compare the strain redistributions that results from different IOLs. For instance, it has been reported that a new intraocular lens design by Alcon Laboratories, Inc. (the AcrySof[®] lens) has been reported to reduce PCO from

the ~40-60% for other lenses to ~10% (Spalton, 1999); thus, not all IOLs are created equal.

Accommodation

To better understand the accommodative process, it is necessary to study other constituents of the accommodative apparatus, including the mechanical interactions between the lens and lens capsule, mechanical properties of the lens, viscoelastic behavior of the lens and lens capsule, zonular tension, and forces generated from contraction of the ciliary muscles. Therefore, a solid understanding of the mechanics of accommodation will require much thought in developing innovative testing techniques, appropriate for the detailed study of each constitutive element of the accommodative apparatus. For instance, special 1D compression tests with glass plates may be used to study the mechanics of the lens, while a biaxial stretching apparatus could be used to study the short-term viscoelasticity of the lens capsule, via stress relaxation tests.

Studies on Human Lens Capsule

The experimental system discussed in Chapter III can also be used to study the multiaxial mechanical behavior of the human lens capsule. This will allow us to describe the general characteristics of the human lens capsule (in a similar way to that done with the porcine lens capsule) and then quantify material properties. Furthermore, human studies will also allow for statistical comparisons between gender, age, and different disease states, such as diabetes. It may then be possible to individualize an optimum IOL design for different people, based on a particular category they may fit in (for example, the IOL designed for diabetics may be different than that designed for non-

diabetics). Additionally, the statistical comparisons between different age groups may provide insight into presbyopia by answering if and how the mechanical properties of the lens capsule change with age. This will have a great impact on the development of an accommodative lens, because it tells whether or not the elderly may have the potential to recover accommodation.

Moreover, human studies will allow us to investigate changes in the strain field and curvature of the lens capsule, due to accommodation and cataract surgery.

Contraction of the ciliary muscles in the porcine eyes could not be induced, in-situ, due to their naturally poor ability to accommodate; thus, human eyes will provide much more insight into the mechanics of the lens capsule during accommodation.

Additionally, it is the strain redistribution from cataract surgery that occurs in human lens capsules (rather than porcine lens capsules) that is of most interest. Therefore, human studies will provide many more possibilities.

CHAPTER VII

CONCLUSION

The mechanics of the lens capsule plays a central role in many causes of visual impairment. For instance, with more than 1.5 million cataract surgeries performed in the U.S. each year and nearly half of these surgeries only providing temporary visual restoration, it is believed that changes in the mechanical environment of the lens capsule (due to the original cataract surgery) cause this secondary loss of vision. Presbyopia (or loss of accommodation) is another visual impairment resulting in part from age-related changes in the mechanics of the lens capsule. Therefore, proper treatment of these causes of visual impairment can only be achieved once the mechanics of the lens capsule is better understood.

As with any mechanics problem, it is necessary to determine the geometry, material properties, and applied loads. Unfortunately, this information has not fully been obtained in previous research. Therefore, the goal of this work was to construct an experimental device capable of altering stresses in the lens capsule, in its intact state within the eye, while measuring 3D geometry and localized surface deformations. This system will be useful in providing data necessary to quantify the regional, multiaxial mechanical behavior of the lens capsule, thus accounting for heterogeneity and anisotropy. In addition, this data can be used in a sub-domain inverse finite element program, along with a constitutive framework appropriate for nonlinear, pseudoelastic biological membranes, to calculate material parameters of the lens capsule. This

experimental device must also provide a way to examine the surface deformations and changes in 3D geometry of the lens capsule that result from various procedures used in cataract surgery. This will provide quantification of changes in stress and strain fields as well as curvature of the lens capsule.

Results show that the meridional and circumferential directions are the principal directions for strain. Additionally, the meridional strain and circumferential strain were the same through most of the anterior lens capsule, reaching maximum strains (with respect to the stress-free reference configuration) of nearly 20%. The only difference found between directional strains was near the equator, where the meridional strain was slightly greater. Preconditioning effects were also found to be significant, as evident from differences between the first and fifth loading and unloading cycles. Thus, it seems that four cycles are necessary to precondition the material, where each of these cycles tends to stress-soften the lens capsule and reduce hysteresis (energy dissipation). Furthermore, a Continuous Circular Capsulorhexis (CCC) with a 5 mm diameter caused an even redistribution of strain from the meridional direction to the circumferential direction. This redistribution achieved its highest magnitude near the edge of the CCC, where the meridional direction experienced retractional strains of up to 20%, while the circumferential direction experienced extensional strains of up to 20%. It is interesting to note that the magnitude of these strains were the same, and even more, any strain at all verifies the concept of a pre-strain in the lens capsule. Furthermore, curvature was found to increase near the edge of the CCC and remain the same near the equator. This is important for it suggests that a hole formed in the anterior lens capsule will

significantly change the curvature of the underlying lens. Therefore, it is likely that the location, size and shape of the hole must be considered in the design of an accommodative intraocular lens.

This thesis presents only part of the results from an on-going effort to rigorously study the mechanics of the lens capsule and its relation to cataract surgery and accommodation (see Fig. 31). Final results from this project should be useful in reducing the occurrence of secondary cataracts by improving capsulotomy and extraction techniques for cataract removal and optimizing the design of intraocular lenses, as well as providing information beneficial in the pursuit of developing an accommodative intraocular lens.

REFERENCES

- Altamirano, D., Mermoud, A., Pittet, N., van Melle, G., Herbort, C.P., 1992. Aqueous humor analysis after Nd:YAG laser capsulotomy with the laser flare-cell meter. *Journal of Cataract and Refractive Surgery* 18, 554-558.
- American Academy of Ophthalmology, 2001. *Cataract in the adult eye. Preferred Practice Pattern* (www.aao.org).
- Andreassen, T.T., Seyer-Hansen, K., Bailey, A.J., 1981. *Biochimica et Biophysica Acta* 677, 313-322.
- Apple, D.J., Ram, J., Foster, A., Peng, Q., 2000. Posterior capsule opacification (secondary cataract). *Survey of Ophthalmology* 45(Suppl 1), S70-S99.
- Assia, E.I., Apple, D.J., Tsai, J.C., Lim, E.S., 1991. The elastic properties of the lens capsule in capsulorhexis. *American Journal of Ophthalmology* 111, 628-632.
- Bailey, A.J., Sims, T.J., Avery, N.C., Miles, C.A., 1993. Chemistry of collagen cross-links: glucose-mediated covalent cross-linking of type-IV collagen in lens capsules. *Journal of Biochemistry* 296, 489-496.
- Barnard, K., Burgess, S.A., Carter, D.A., Wooley, D.M., 1992. Three-dimensional structure of type IV collagen in the mammalian lens capsule. *Journal of Structure Biology* 108, 6-13.
- Burd, H.J., Judge, S.J., Cross, J.A., 2002. Numerical modeling of the accommodating lens. *Vision Research* 42, 2235-2251.
- Chatterjee, C., Chong, E.K.P., 1997. Efficient algorithms for finding the centers of conics and quadrics in noisy data. *Pattern Recognition* 30(5), 673-684.
- Cohen, M., Urdanivia, E., Surma, M., Wu, V.Y., 1980. *Biochemistry, Biophysics Research and Communication* 95, 765-769.
- David, G., Humphrey, J.D., 2004. Redistribution of stress due to a circular hole in a nonlinear anisotropic membrane. *Journal of Biomechanics* (accepted 4 Dec. 2003)
- Delange, S.L., 2002. *Biomechanics of the lens capsule. M.S. Thesis*, Texas A&M University, College Station.

- Emery, J., 1999. Capsular opacification after cataract surgery. *Current Opinion in Ophthalmology* 10, 73-80.
- Fisher, R.F., 1969a. Elastic content of the human lens capsule. *Journal of Physiology* 201, 1-19.
- Fisher, R.F., 1969b. The significance of the shape of the lens and capsular energy changes in accommodation. *Journal of Physiology* 201, 21-47.
- Fisher, R.F., Pettet, B.E., 1972. The postnatal growth of the capsule of the human crystalline lens. *Journal of Anatomy* 112, 207-214.
- Fung, Y.C., 1993. *Biomechanics: Mechanical Properties of Living Tissue*. Second Edition. Springer-Verlag, New York.
- Gander, W., Golub, G.H., Strebel, R., 1994. Least squares fitting of circles and ellipses. *BIT* 34, 556-577.
- Haddad, A., Bennett, G., 1988. Synthesis of lens capsule and plasma membrane glycoprotein by lens epithelial cells and fibers in the rat. *American Journal of Anatomy* 183, 212-225.
- Hayashi, K., Hayashi, H., Nakao, F., Hayashi, F., 2002. Posterior capsule opacification after cataract surgery in patients with diabetes mellitus. *American Journal of Ophthalmology* 134, 10-16.
- Hollick, E.J., Spalton, D.J., Meacock, W.R., 1999. The effect of capsulorhexis size on posterior capsular opacification: one-year results of a randomized prospective trial. *American Journal of Ophthalmology* 128, 271-284.
- Humphrey, J.D., 2002. *Cardiovascular Solid Mechanics: Cells, Tissues, and Organs*. Springer-Verlag, New York.
- Kaufman, P.L., 1992. *Adler's Physiology of the Eye: Accommodation and Presbyopia: neuromuscular and biophysical aspects*. Ninth Edition. Mosby Year Book, St. Louis.
- Koretz, J.F., 1994. *Principles and Practice of Ophthalmology: Accommodation and presbyopia*. WB Saunders Company, Philadelphia.
- Krag, S., Andreassen, T.T., 2003. Mechanical properties of the human lens capsule. *Progress in Retinal and Eye Research* 22, 749-767.
- Krag, S., Danielsen, C.C., Andreassen, T.T., 1998. Thermal and mechanical stability of the lens capsule. *Current Eye Research* 17, 470-477.

- Krag, S., Olsen, T., Andreassen, T.T., 1997a. Biomechanical characteristics of the human anterior lens capsule in relation to age. *Investigative Ophthalmology and Visual Science* 38, 357-363.
- Krag, S., Thim, K., Corydon, L., 1993. Strength of the lens capsule during hydroexpression of the nucleus. *Journal of Cataract Refractive Surgery* 19, 205-208.
- Krag, S., Thim, K., Corydon, L., 1997b. Diathermic capsulotomy versus capsulorhexis. *Journal of Cataract Refractive Surgery* 23, 86-90.
- Marcantonio, J.M., Rakic, J.M., Vrensen, G.F.J.M., Duncan, G., 2000. Lens cell populations studied in human donor capsular bags with implanted intraocular lenses. *Investigative Ophthalmology and Visual Science* 41, 1130-1141.
- Monnier, V.M., Stevens, V.J., Cerami, A., 1979. Nonenzymatic glycosylation, sulfhydryl oxidation, and aggregation of lens proteins in experimental sugar cataracts. *Journal of Experimental Medicine* 150, 1098-1107.
- Mullins, L., Tobin, N.R., 1957. Theoretical model for the elastic behavior of filler-reinforced vulcanized rubbers. *Rubber Chemistry and Technology* 30, 551-571.
- Ohata, H., Tanaka, K., Maeyama, N., Yamamoto, M., Momose, K., 2001. Visualization of elementary mechanosensitive Ca^{2+} spots, in bovine lens epithelial cells. *Journal of Physiology* 532(Pt 1), 31-42.
- Rafferty, N.S., Goosens, W., 1978. Growth and aging of the lens capsule. *Growth* 42, 375-389.
- Sacks, M.S., Chuong, C.J., Templeton, G.H., and Peshock, R., 1993. In vivo 3-D reconstruction and geometric characterization of the right ventricular free wall. *Annals of Biomedical Engineering* 21, 263-275.
- Sacks, M.S., David, A.V., Raghavan, M.L., Federle, M.P., Webster, M.W., 1999. In vivo three-dimensional surface geometry of abdominal aortic aneurysms. *Annals of Biomedical Engineering* 27, 469-479.
- Saika, S., Miyamoto, T., Ishida, I., Obnishi, Y., Ooshima, A., 2003. Osteopontin: A component of matrix in capsular opacification and subcapsular cataract. *Investigative Ophthalmology and Visual Science* 44, 1622-1628.
- Salzmann, M., 1912. *The Anatomy and Histology of the Human Eyeball in the Normal State, Its Development and Senescence*. Chicago University Press, Chicago, p. 165.

- Schnider, S.L., Kohn, R.R., 1980. Glucosylation of human collagen in aging and diabetes mellitus. *Journal of Clinical Investigation* 66, 1179-1183.
- Seland, J.H., 1974. Ultrastructural changes in the normal human lens capsule from birth to old age. *Acta Ophthalmologica* 52, 688-706.
- Seshaiyer, P., Hsu, F.P.K., Shah, A.D., Kyriacou, S.K., Humphrey, J.D., 2001. Multiaxial mechanical behavior of human saccular aneurysms. *Computer Methods in Biomechanics and Biomedical Engineering* 4, 281-290.
- Spalton, D.J., 1999. Posterior capsular opacification after cataract surgery. *Eye* 13, 489-492.
- Travers, M.J., 1990. Structural correlates of shape change in the primate crystalline lens. Ph.D. Thesis, The City University, London.
- Turner, D.A., Anderson, I.J., Mason, J.C., 1999. An algorithm for fitting an ellipsoid to data. University of Huddersfield, Queensgate.
- Vaughn, D.G., Asbury, T., Riordan-Eva, P., 1995. *General Ophthalmology*, 14th Edition. Appleton and Lange, Norwalk, Connecticut.
- Weale, R.A., 1963. New light on old eyes. *Nature* 198, 944-946.
- Weeber, H.A., 1999. Effect of lens stiffness on accommodative amplitude. *Investigative Ophthalmology and Visual Science* 40, S361 (abstract no. 1913).
- Yang, X., Zou, L., Binrong, M., Dong, D., Dai, H., Lu, X., 1998. Tensile strength of lens capsules in eye-bank eyes. *Journal of Cataract Refractive Surgery* 24, 543-546.
- Young, R.W., Ocumpaugh, D.E., 1966. Autoradiographic studies on the growth and development of the lens capsule in the rat. *Investigative Ophthalmology and Visual Science* 5, 583-593.

VITA

Name: Mark Richard Heistand

Permanent address: 14056 Mint Trail
San Antonio, TX 78232

Degree and date
to be conferred: Master of Science, 2004

Date of birth: March 5, 1978

Education: Abilene Christian University
Abilene, TX
Bachelor of Science in Engineering Physics, 2001

Texas A&M University
College Station, TX
Bachelor of Science in Mechanical Engineering, 2001

Texas A&M University
College Station, TX
Master of Science in Biomedical Engineering, 2004